

Elsevier required licence: © <2022>. This manuscript version is made available under the CC-BY-NC-ND 4.0 license <http://creativecommons.org/licenses/by-nc-nd/4.0/>

The definitive publisher version is available online at

[\[http://doi.org/10.1016/j.addma.2022.103145\]](http://doi.org/10.1016/j.addma.2022.103145)

Instantaneous and long-term mechanical properties of Polyethylene Terephthalate Glycol (PETG) additively manufactured by pellet-based material extrusion

Thomas Romeijn^{ab*}, Michael Behrens^b, Gavin Paul^b and Dongbin Wei^b

^a Mineral Technologies, 11 Elysium Road, Carrara QLD 4211, Australia

^b Faculty of Engineering and Information Technology, University of Technology Sydney, NSW 2007, Australia

*Phone number: +61 7 5569 1300, E-mail: Thomas.Romeijn@mineraltechnologies.com

Abstract

Polyethylene Terephthalate Glycol (PETG) is a highly popular feedstock for extrusion-based additive manufacturing. While data are available on the instantaneous properties of additively manufactured PETG, few research have been done on forecasting the creep behaviour of additively manufactured PETG while accounting for the material altering effects of ageing. This research article aims to enhance the understanding of both the instantaneous and time-dependent mechanical properties of additively manufactured PETG through a series of tensile, FEA simulations, Dynamic Mechanical Analysis (DMA), and two types of creep experiments. The details of experimental and mathematical calculations of the instantaneous and time-dependent properties of additively manufactured PETG are provided. Nine independent material parameters have been determined including three Young's moduli, three shear moduli and three Poisson's ratios, to fully quantify an orthotropic material model of additively manufactured PETG. The printed material exhibited a Young's modulus that is 86.5% of the theoretically possible value in direction 1, a Young's modulus in direction 2 is 66.0% of the theoretical optimum, and a Young's modulus in direction 3 is within 1% of its theoretical maximum. In addition to reporting the creep behaviour of PETG, the novel application of the Time-Temperature Superposition Principle (TTSP) to additively manufactured PETG has been shown to produce an age-affected creep prediction for up to 3.88 years based on samples aged for 221 h and at 23 °C. The methodology and data models have been found to enable predictions for other ages and temperatures. It was concluded that the application of the TTSP creep methodology was limited by the creep test temperature, 60 °C, after which the material began to behave in a non rheologically-simple manner.

Keywords

Polyethylene Terephthalate Glycol (PETG), material extrusion, tensile properties, Time-Temperature Superposition Principle (TTSP), creep, aging

1 Introduction

The additive manufacturing process has cemented itself as an increasingly viable alternative to traditional manufacturing methods of components. Especially the material extrusion method of additive manufacturing [1] where a layer of heated, viscous feedstock is precisely deposited on a previously deposited and solidified layer, has been used extensively to manufacture a large gamut of components. This method, also known as Fused Filament Fabrication (FFF), where the viscous feedstock partially dissipates heat through the previous layer, results in uneven reheating of regions within the material. Furthermore, the deposited feedstock often fails to uniformly adhere to the previous layer resulting in voids in the printed material [2], even when the densest print method is selected and extrusion problems are avoided. Overall, the FFF process leads to anisotropic material properties, even when using isotropic feedstock, as the build process and the feedstock's characteristics both affect the final material properties [3].

The large number of selectable parameters in the FFF process, referred to as tool path parameters or print parameters, further affect the material properties of FFF materials. Significant research efforts have been undertaken in this area, as summarised by Dizon et al. [4]. The tool path parameters that have the largest influence on the FFF-printed material's strength [5, 6] are listed in the first column of Table 1, where alternative nomenclature of the parameters are given in brackets. Some tool path parameters are visualised in Figure 1.

Tool path parameters	Value in solid printing
Number of contours (number of shells)	No contours
Raster angle (raster fill angle / raster orientation)	0° (along the x-direction)
Road width (bead width/filament width)	5 mm
Layer thickness (slice thickness, slice height)	2 mm
Air gap (raster-to-raster air gap)	No air gap, solid print
Infill (raster pattern)	No infill
Build orientation (build direction / part print direction)	Printed on the x-y plane

Table 1: Tool path parameters used in the solid print

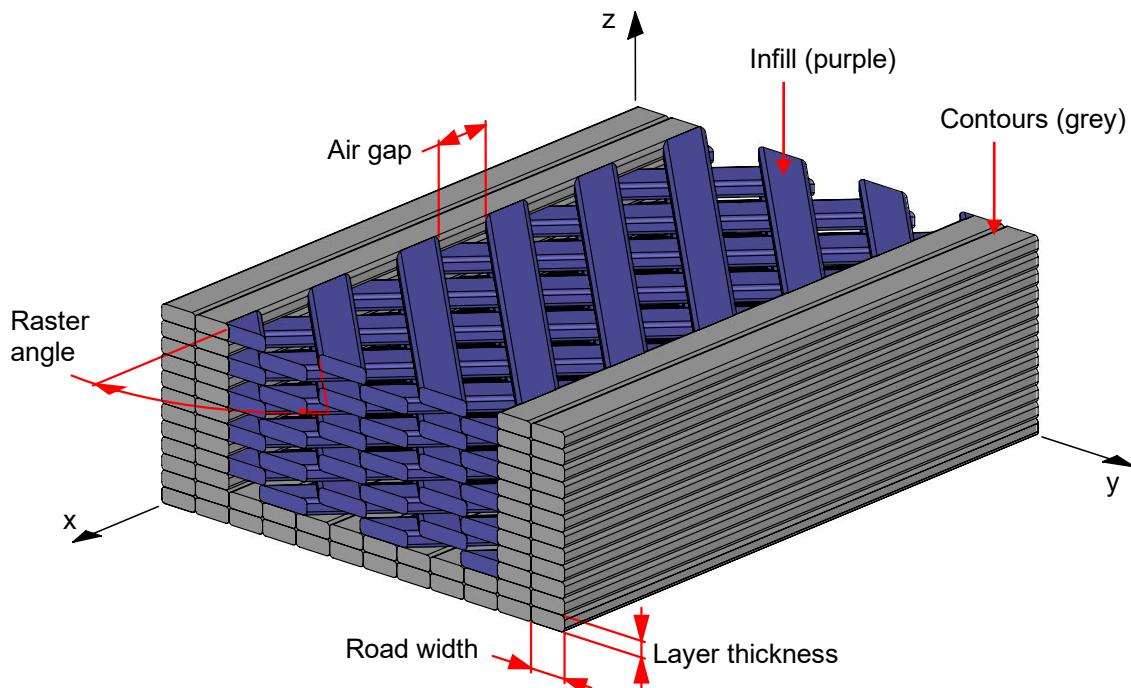


Figure 1: Visualisation of the tool path parameters

Several material models have been proposed to best characterise an FFF-produced material. An orthotropic material model, where the material properties differ along three mutually perpendicular principal planes, has been frequently used [3, 7-10]. The orthotropic material model requires nine independent material constants to fully quantify the model: three tensile moduli (E_1 , E_2 , E_3), three Poisson's ratios (ν_{12} , ν_{23} , ν_{31}) and three shear moduli (G_{12} , G_{13} , G_{23}).

This article aims to quantify the mechanical properties of FFF-manufactured Polyethylene Terephthalate Glycol (PETG), an amorphous copolyester and a glycol modified version of Polyethylene Terephthalate (PET). PET has been the world's most widely produced plastic [11] due to favourable ductility, chemical stability, processability and recyclability [12]. Especially its property to crystallise at processing temperatures and high strains is valued as it improves the material's rigidity, gas permeability and strength due to anisotropic material behaviour [13]. The glycol modified version of Polyethylene Terephthalate, PETG, exhibits relatively low levels of crystallinity [14] making it useful in applications where the translucency of the material cannot be compromised due to the formation of crystalline regions, such as large display panels [13]. PETG has become one of the most commonly used FFF feedstock in recent years [11] which makes investigations into its instantaneous and long-term properties compelling.

The instantaneous mechanical properties of FFF-manufactured PETG, are quantified in this article by calculating the nine orthotropic material constants based on a so-called 'solid' print. Such instantaneous mechanical properties of solid prints have been investigated by other researchers [2, 9, 15-17] but often the raster angle was alternated between layers, such as a $0^\circ/90^\circ$ or $45^\circ/-45^\circ$ configuration. The solid print proposed herein, with its tool path parameters set to the values in the second column of Table 1, results in a material comprised of uniformly parallel roads. A unit cube of such a material, with the desired nine material constants as shown in Figure 2, is the simplest representation of the instantaneous mechanical properties of FFF-manufactured PETG.

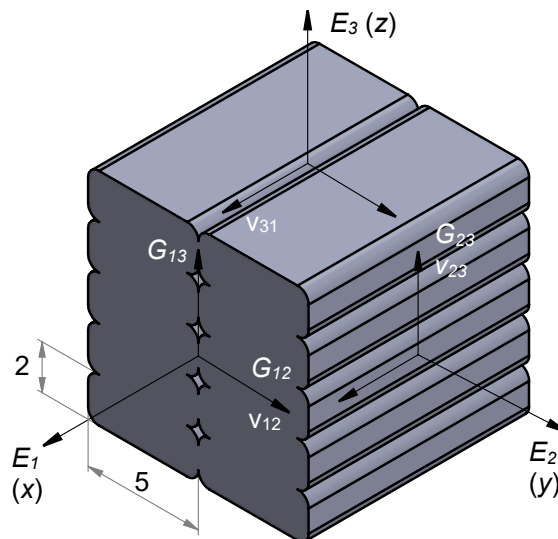


Figure 2: The nine independent material constants for a solid-printed unit cube

The knowledge of instantaneous mechanical properties is important, but it is insufficient for designing additively manufactured products and components that are expected to have long service lives. The time-dependent effects of creep, the continuous deformation of a polymer under a constant load, and the effects of ageing, where material properties change as the material moves towards a thermodynamical equilibrium over time [18-20], need to also be accounted for.

Several researchers have investigated the effects of creep on additively manufactured polymer components [21-26] but very few accounted for the effects of ageing [27]. Moreover, while several research teams reported the creep response of additively manufactured materials [21-26], limited data are available that could be used to predict the creep behaviour for time spans longer than those that can be practically tested for. In other words, to fully quantify additively manufactured materials, the instantaneous mechanical properties need to be supplemented by predictions of its time-dependent properties; a creep behaviour prediction that accounts for the material altering effects of ageing. Currently, very little data are available to forecast the creep behaviour of additively manufactured materials generally, and PETG specifically. This research article aims to improve the understanding of the prediction of creep behaviour of additively manufactured PETG by pellet-based material extrusion.

This article is organised as follows. Section 2 discusses the background behind the measurement and calculation of the instantaneous and time-dependent properties. The required experiments that follow are described in Section 3. The results are found and discussed in Section 4, and then Section 5 draws a conclusion.

2 Background

This section details the background and principles behind the instantaneous and time-dependent assessment of the material properties of additively manufactured PETG. The types of experiments required to support these principles are mentioned at the end of this section.

2.1 Instantaneous mechanical properties

The Hooke's law relating stresses to strains, $\{\varepsilon\} = [S]\{\sigma\}$, for an orthotropic material occurs via the compliance matrix $[S]$, as shown in Eq. (1) [9].

$$[S] = \begin{bmatrix} \frac{1}{E_1} & -\frac{\nu_{21}}{E_2} & -\frac{\nu_{13}}{E_1} & & & \\ -\frac{\nu_{21}}{E_2} & \frac{1}{E_2} & -\frac{\nu_{23}}{E_2} & & & \\ -\frac{\nu_{13}}{E_1} & -\frac{\nu_{23}}{E_2} & \frac{1}{E_3} & & & \\ & & & \frac{1}{G_{23}} & & \\ & & & & \frac{1}{G_{13}} & \\ & & & & & \frac{1}{G_{12}} \end{bmatrix} \quad (1)$$

Directions 1, 2 and 3 herein align with the x, y and z axes of Figure 2.

Therefore, to quantify the orthotropic model for solid FFF-printed PETG, a series of tensile tests can determine the three Young's moduli (E_1, E_2, E_3) and three Poisson's ratios ($\nu_{13}, \nu_{21}, \nu_{23}$) according to the ASTM D3039 standard [28]. Currently, no uniform standard exists to determine the three shear moduli (G_{12}, G_{13}, G_{23}) of additively manufactured materials so research teams have applied a variety of closely related standard such as ASTM D3518 [2, 7], D3846 [2, 29] and ASTM D7264 [30]. Additionally, several researchers [9, 10, 31-34] have calculated the shear moduli based on other Young's moduli and Poisson's ratios and this approach will be followed in this research article. [28]

The stress distribution in a thin tensile sample can be approximated by a state of plane stress, where the stress and shear normal to the sample's largest face are assumed to be zero. As

derived by Zhao [31], the G_{12} shear modulus of a tensile sample positioned in the 1-2 plane, can be derived as,

$$G_{12} = \left(\frac{4}{E_{12_{45^\circ}}} - \frac{1}{E_1} - \frac{1}{E_2} + \frac{2\nu_{12}}{E_1} \right)^{-1} \quad (2)$$

Where $E_{12_{45^\circ}}$ is the Young's modulus of a tensile sample in the 1-2 plane extracted at a 45° off-angle direction. Eq. (2) can be adapted to determine the other two shear moduli, G_{13} , G_{23} , for tensile samples positioned in the 1-3 and 2-3 plane respectively:

$$G_{23} = \left(\frac{4}{E_{23_{45^\circ}}} - \frac{1}{E_2} - \frac{1}{E_3} + \frac{2\nu_{23}}{E_2} \right)^{-1} \quad (3)$$

$$G_{13} = \left(\frac{4}{E_{13_{45^\circ}}} - \frac{1}{E_1} - \frac{1}{E_3} + \frac{2\nu_{13}}{E_1} \right)^{-1} \quad (4)$$

The so-called 'reciprocal relationships' [35], given in Eq. (5), explain the relationship between the various Young's moduli and Poisson's ratios.

$$\begin{aligned} \frac{\nu_{12}}{E_1} &= \frac{\nu_{21}}{E_2} \\ \frac{\nu_{23}}{E_2} &= \frac{\nu_{32}}{E_3} \\ \frac{\nu_{13}}{E_1} &= \frac{\nu_{31}}{E_3} \end{aligned} \quad (5)$$

To fully quantify the instantaneous orthotropic model, three tensile tests are required to determine the three Young's moduli (E_1 , E_2 , E_3), henceforth referred to as the 'E₁, E₂, E₃ experiments'. Additionally, three tensile tests on off-angled samples are further needed to determine the three shear moduli (G_{12} , G_{13} , G_{23}), referred to as the 'G₁₂, G₁₃, G₂₃ experiments'. The relative position of all sets of tensile samples are illustrated in Figure 3, using the print parameters as listed in the second column of Table 1, where a 10× enlarged example of the road direction is also provided for clarity.

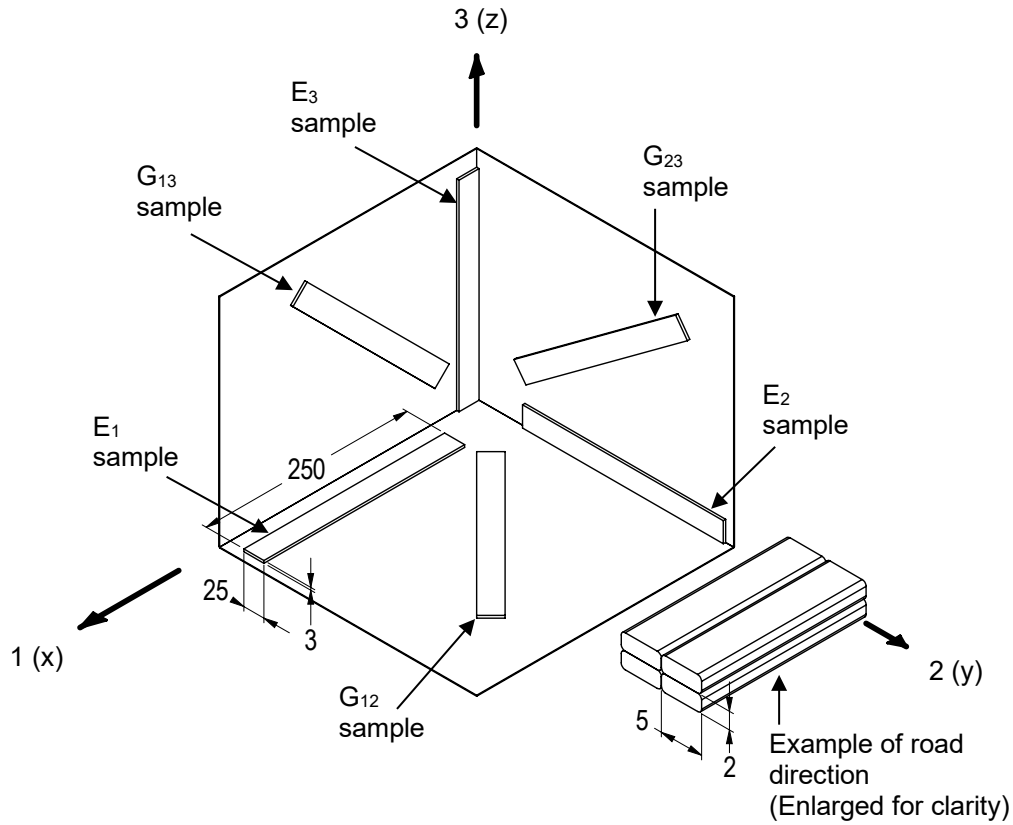


Figure 3: The relative position of the 6 tensile samples to the print direction

Finally, three Poisson's ratios are required to fully quantify the instantaneous orthotropic model. The Poisson's ratios are defined as the negative fraction of the transverse strain to the axial strain which, using the E_1 , E_2 , E_3 samples, resulting in the following:

$$\begin{aligned}
 E_1 \text{ sample: } \nu_{12} &= -\frac{\varepsilon_2}{\varepsilon_1} \\
 E_2 \text{ sample: } \nu_{23} &= -\frac{\varepsilon_3}{\varepsilon_2} \\
 E_3 \text{ sample: } \nu_{31} &= -\frac{\varepsilon_1}{\varepsilon_3}
 \end{aligned} \tag{6}$$

All three Poisson's ratios (ν_{12} , ν_{23} , ν_{31}) were measured in-plane with the DIC unit facing the largest side of the sample.

2.2 Time-dependent properties

2.2.1 Different accelerated creep testing methodologies

Several techniques have been established in literature to determine the creep behaviour of a polymer beyond practical experimental durations. Based on the theory of free volume [18], the principle of all such accelerated creep testing methods is to impose a state of increased free volume energy in a test sample. This artificially imposed energy state simulates the free volume energy state the sample would have naturally evolved into over time. The method of imposing this new free volume energy state differs between the various accelerated creep methodologies but is limited to an increase in temperature, referred to as the Time-Temperature Superposition Principle (TTSP), an increase in stress, referred to as the Time-Stress Superposition Principle (TSSP), or a combination of both, referred to as the Time-Temperature-Stress Superposition Principle (TTSSP). The well-established TTSP methodology was used in this research for the creep prediction for additively manufactured PETG.

Leaderman [36] was one of the first to recognise that a portion of the creep curve tested at a low temperature is identical to the shape of the creep curve measured at an elevated temperature and that a constant value, known as the ‘temperature shift factor’, accounts for the difference in location of the curves in a strain-time graph. This Time-Temperature Superposition Principle (TTSP), furthered by pioneers such as Tobolsky & Andrews [37], allows for the conversion of the results from several short-term creep tests at elevated temperatures, via the temperature shift factor, into a prediction of long-term creep response at a single temperature. The time span of this creep response, the so called ‘master curve’, then greatly exceeds that of the input creep tests. In other words, the theory of TTSP dictates that an increasing in temperature is equivalent to stretching the real time of the viscoelastic creep response [38, 39]. If the creep curves are indeed superimposable, the material is defined as being ‘rheologically simple’. The creation of a master creep curve is thus an avenue to predict the creep behaviour of polymers over time periods that are far too long to test practically.

2.2.2 Application constraints of the accelerated creep methodologies

The behaviour of a viscoelastic material, such as additively manufactured PETG, can be distinguished into two regions: a linear and non-linear viscoelastic region. The theory of linear viscoelastic behaviour is based on the Boltzmann’s Superposition Principle which states that each stress contribution acts independently and the strains can be added linearly [40, 41]. ASTM D2990 [42] explains the principle via the total strain $\varepsilon(t)$ as follows,

$$\varepsilon(t) = J(t)\sigma_0 + J(t)(t - t_1)(\sigma_1 - \sigma_0) + \dots J(t)(t - t_n)(\sigma_n - \sigma_{n-1}) \quad (7)$$

Where J is the creep compliance (time-dependent reciprocal of modulus), σ_0 is the applied stress (initial), and t is the time (initial).

As is clear from equation (7), each additional increase in stress adds to the strain independently of the previously applied stresses. The linear viscoelastic behaviour thus assumes that the creep compliance (J) or it’s reciprocal; the creep modulus, is only a function of time and not of other variables such as stress or strain [43-45]. As soon as the modulus is affected by other variables besides time, the Boltzmann’s Superposition Principle is no longer valid, and the material has thus entered the non-linear viscoelastic range. Therefore, for strains below a critical point, a slowly increasing strain will deliver a constant modulus response but for strains beyond the critical point, the modulus becomes strain dependent. At this strain magnitude, Boltzmann’s Superposition Principle does not apply anymore thereby marking the end of the LVR [41].

Such a so-called ‘strain sweep’ can be executed by subjecting a sample to a Dynamic Mechanical Analysis (DMA) experiment where a sample, using a variety of clamping options, undergoes a reciprocal deformation with a fixed frequency but a slowly increasing amplitude. The outputs of such a strain sweep are two moduli of the material. The so called ‘storage modulus’ (E') indicates how much of the deformation energy is stored by the material whereas the ‘loss modulus’ (E'') is a measure of how much energy is dissipated [46]. The strain magnitude signalling the end of the linear viscoelastic range is found when the storage modulus has diverged from the plateaued value by 5% [47].

Such a DMA experiment, in accordance with ASTM D5023, was performed in this research with the aim of determining the load case that is close to the end of the linear viscoelastic range. This load was then applied to subsequent creep experiments to derive a creep prediction.

2.2.3 Ageing in accelerated creep and the snap-shot assumption

Polymers continue their glass formation by striving for a thermodynamic state of equilibrium after a transition from viscous state into solid form [18]. This process continuously alters the properties of polymers and is known as 'physical ageing'.

The effect of the ageing process is that when testing for time-dependent properties, the material, and thus the creep behaviour, changes during the creep experiments. As such, ageing invalidates the Boltzmann's superposition principle on which TTSP and its derivatives are based [18]. Still, ageing can be separated from creep by adhering to the condition: the creep tests underlying the creep prediction are short enough in duration to assume that the effects of ageing on the creep response are negligible [1]. This so called 'snap-shot assumption' states that the creep experiment's duration (t) shall remain below 10 % of the sample's age (t_e). This assumption then separates the ageing effects from the creep results. Thus, the material does not change during creep testing so Boltzmann's superposition principle still applies.

As first shown by Struik [18] and applied by other researchers, the material altering effects of ageing can be reversed by subjecting the material to a heat treatment process. In this process, the material is heated to temperatures slightly above its glass transition temperature, held there for some time, and subsequently allowed to cool. This process is often referred to as 'resetting the ageing clock' of the material.

Since the creation of the master creep curve relies on the Boltzmann's Superposition Principle, it is important to derive the creep load in the DMA experiments for the most age-affected material. Otherwise, the possibility exists that the Boltzmann's Superposition Principle fails to apply to some creep tests, rendering the master creep curve invalid. Given that the principle behind a master creep curve is that information gained from an aged sample is equivalent to that gained from an elevated temperature creep test, the creep load should be determined by DMA experiments using samples at the highest practical test temperature. This DMA testing temperature has been selected to be 5 °C below the glass transition temperature of the PETG, resulting in a test temperature of 75 °C.

2.2.4 Effective time

To create the master curve, a series of creep experiments are required, all adhering to the snap-shot assumption, at different temperatures but all having the same age. This series of creep tests is henceforth referred to as the 'temperature creep experiments'. It should be realised that these temperature creep experiments will lead to a master curve of additively manufactured PETG which does not age over time; a so called 'momentary' creep master curve. This statement follows from the fact that the snap-shot assumption excludes ageing from the temperature creep experiments on which the master curve is based. Given that ageing is such an essential aspect of the long-term behaviour of polymers, it is imperative to include ageing after the momentary master curve has been composed.

The factor by which the creep curves of an ageing material are shifted horizontally is called the acceleration factor (a_e) and this factor decreases with time. This decrease can be approximated by the following power law equation, which has been shown to remain valid for tens of years [18],

$$a_e(t) = \left(\frac{t_e}{t_e + t} \right)^\mu \quad (8)$$

where t is the creep time, or duration of a creep experiment, t_e is the ageing time, or the age of the

sample when the creep experiment commences, and μ is the ageing shift rate.

The ‘ageing shift rate’ (μ) and this variable has been found to be constant over long periods of time and for a wide range of temperatures. Eq. (8) indicates that the ageing shift rate (μ) completely characterises the ageing of a sample.

The acceleration factor (a_e) can be used to introduce an ‘effective time’ as older creep curves are less ‘eventful’ than creep curves determined at a more recent point in time. By using the acceleration factor, based on the constant ageing shift rate, this ‘effective time’ can then be related to real time. This is key to reintroduce ageing in a momentary creep master curve; applying a shift to the master curve based on the effective time of the sample, which in turn is determined via the acceleration factor and ageing shift rate, at a desired age.

To determine the ageing shift rate, data on the creep response of samples with a range of different ages, but at a single temperature, are needed. Again, the snap-shot assumption needs to be adhered to so that the material remains unaffected by the ageing process during the experiments. This series of creep experiments is henceforth referred to as the ‘ageing creep experiments’.

3 Materials and Methods

Based on the methodologies explained above the characterisation of the material properties of additively manufactured PETG will require four sets of experiments. Two sets of tensile tests are needed: the E_1, E_2, E_3 experiments and G_{12}, G_{13}, G_{23} experiments, shown in Figure 4. Through several steps, the outcomes of these experiments are combined to deliver the nine material constants required for the orthotropic material model. The experimental instantaneous properties were subsequently compared to theoretical values through a Finite Element Analysis (FEA) simulation of a homogenised unit cell of the printed material. This unit cell was derived from measurements of the cross-sectional shape of the road. The experimental measurement supported by a theoretical benchmark thereby quantified the instantaneous material model of additively manufactured PETG. To round out the instantaneous material properties investigation, the densities of the feedstock and extruded material were measured.

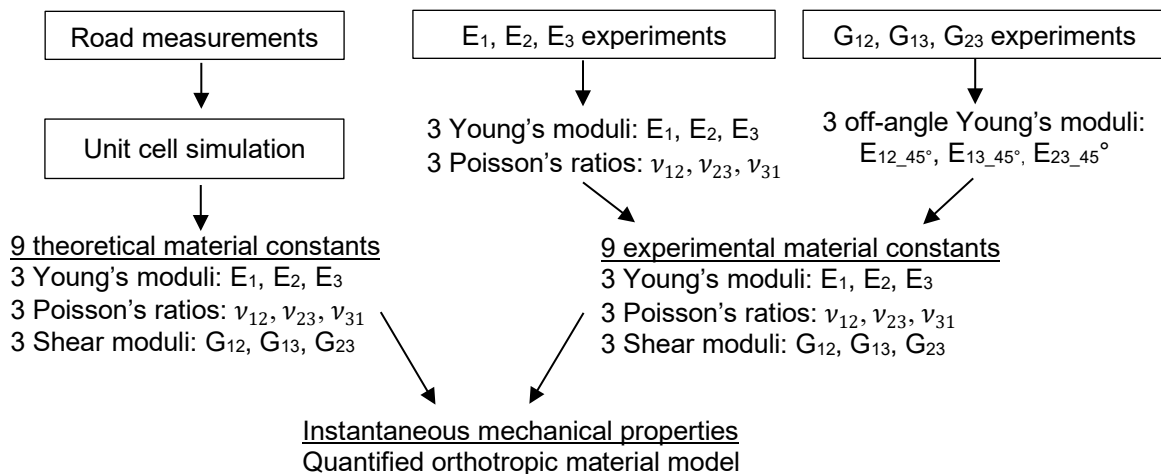


Figure 4: Workflow to characterise the instantaneous mechanical properties

To derive the time-dependent mechanical properties, firstly a series of DMA experiments at a test temperature of 75 °C, shown in Figure 5, will determine the load to be applied in the subsequent creep analyses. Using this load case, the material’s creep behaviour will be measured at different temperatures; the temperature creep experiments, and utilising the same load case, the material’s

creep behaviour will be assessed at various ages; the ageing creep experiments. These two series of creep experiments are also shown in Figure 5. Through a series of intermediate steps, an ageing affected master curve can then be created, producing a creep prediction and thereby quantifying the time-dependent properties of additively manufactured PETG.

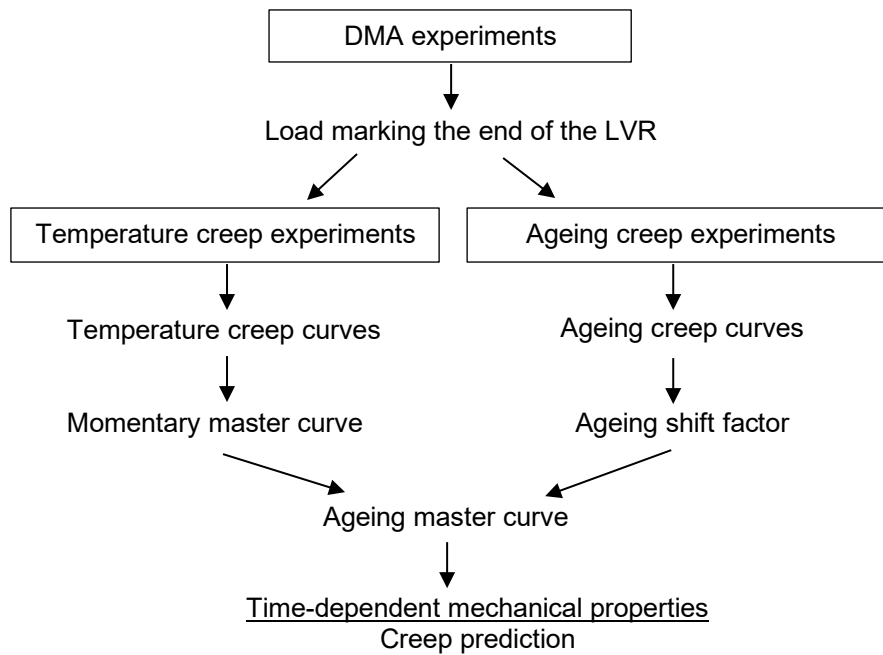


Figure 5: Workflow to characterise the time-dependent mechanical properties

3.1 Material

The glycol-modified polyethylene terephthalate (PETG) used in this research article is SK Chemicals' SKYGREEN® S2008, with a glass transition temperature of 80 °C. This material was used in a bespoke 3D printer, developed by the University of Technology Sydney to provide a significantly larger-than-standard build volume of roughly 0.7 m³. The whole printer is a bespoke system, using a screw extruder to prepare standard injection moulding pellets of the feedstock for extrusion through a 5 mm nozzle mounted on an industrial robotic arm. Due to the highly bespoke nature of the 3D printer, a fully bespoke slicing solution was developed to suit the application. The base shapes from which the various test samples were extracted were printed using the following print parameters listed in Table 2.

Print parameters	Value in test samples
Extrusion Temperature	220 °C
Bed Temperature	Unheated
Enclosure Temperature	38 °C
Volumetric Flow Rate	≈ 500 mm ³ /s
Road width	5 mm
Layer thickness	2 mm

Table 2: Print parameters used in the creation of the test samples

3.2 Sample preparation

3.2.1 Tensile samples

ASTM D3039 recommends several sample dimensions and a sample measuring 25×250×3 mm was selected for use in the E₁, E₂, E₃ and G₁₂, G₁₃, G₂₃ experiments. For the E₁, E₂, E₃ experiments, 8 samples per test condition were tested, and for the G₁₂, G₁₃, G₂₃ experiments 4

samples per test condition were used.

Several PETG base shapes were printed from which the tensile samples were extracted. A block shape was required for the E_2 samples, and a vase structure was printed to suit the E_3 samples. A flat plate with a thickness of two roads allowed the extraction of the E_1 and G_{12} sample sets, as shown in Figure 6. For the remaining off-angled samples, G_{13} , G_{23} , an inclined shape was printed. Sufficiently large base shapes were printed to allow that, for each test series, all samples could be extracted from a single base shape. This minimised differences between test samples. Moreover, the different base shapes were printed in succession to minimise the variation between base shapes.



Figure 6: The printed base shapes for the E_1 and G_{12} tensile samples

Each base shape was cut with a bandsaw into oversized strips. The strips were subsequently fly cut to the correct thickness, then milled, using small passes and flood coolant, to the final 250x25 mm dimensions. The translucent nature of the material allowed the machinist to ensure the location of the bonding regions inside the samples remained consistent within each sample set. After the machining of the base shape into individual samples, each sample's cross-sectional dimensions were measured at three locations along its length using a digital vernier calliper to two significant figures. In addition to being required for subsequent analyses, the resulting series of dimensions allowed the calculation of the cross-sectional Coefficient of Variation (CoV) to assess the quality of the subtractive step. When this quality metric was applied to the first batch of samples, it was found that the highest cross-sectional CoV in any direction was 1.43 %. This low value testifies to the quality of work of the machining department and corroborates the quality of the sample preparation overall.

The ASTM D3039 standard allows the application of end tabs to improve the likelihood of the sample failing within the gage area. The tabs were applied to the sample sets and had the following properties:

- Tab material: Single-sided PCB, FR4, which is an epoxy resin with glass-fibre reinforcements. The copper was ensured to be on the non-adhesive side

- Tab dimensions: 25×44×1.6 mm
- Tab chamfer: 1.3×6 mm, resulting in a 12.2° chamfer angle

Four tabs were adhered to each sample using 3M Instant Adhesive PR100, with a layer thickness within 0.5-1.3 mm. The glue was allowed to cure for two days. Completed samples of the E₁, E₂, E₃ experiments are shown in Figure 7.

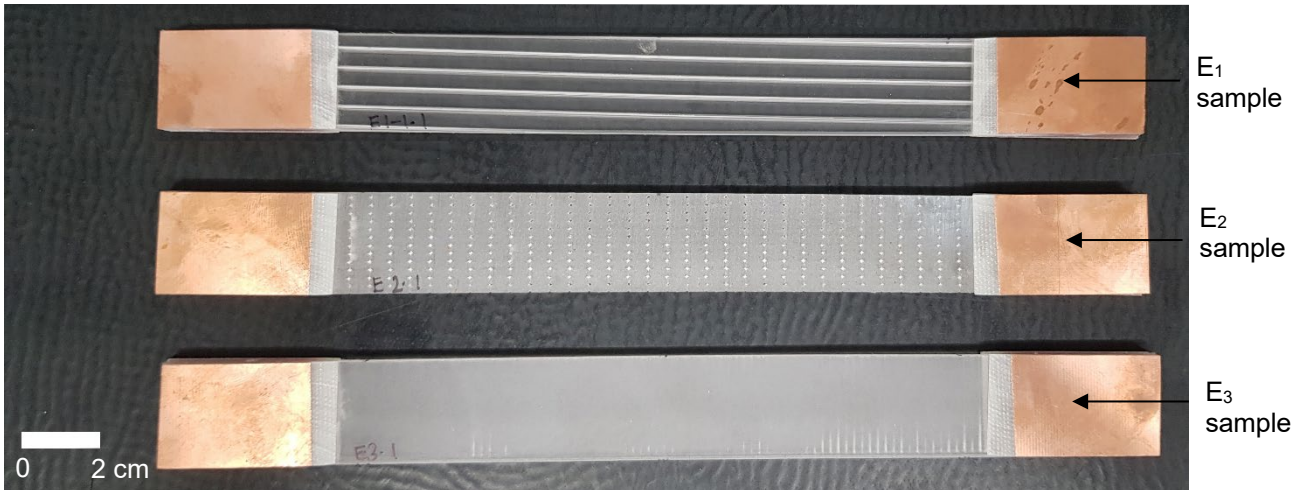


Figure 7: An E₁, E₂ and E₃ tensile sample

To enable the DIC unit to measure the displacement of points on the samples, each gage area of the sample was given a white basecoat of paint, followed by an uneven coat of black spray paint. The latter ensured that each gage area has a randomised black dot pattern which can be recognised as a reference frame by the DIC system.

3.2.2 Road dimensions samples

The cross-sectional dimensions of the roads were determined using the same E₂ samples as described in Section 3.2.2 for the tensile experiments.

3.2.3 Density samples

The density measurements of additively manufactured PETG were performed on a roughly 30 mm section of the E₂ and E₃ samples used in the tensile experiments, as described in Section 3.2.2.

3.2.4 DMA samples

For the DMA test series, rectilinear 60×12.5×1 mm test samples were used. The position of the sample relative to the road direction is illustrated in Figure 8. The samples were printed using the same print parameters and machining processes used for the instantaneous tensile samples. A total of 4 samples were produced.

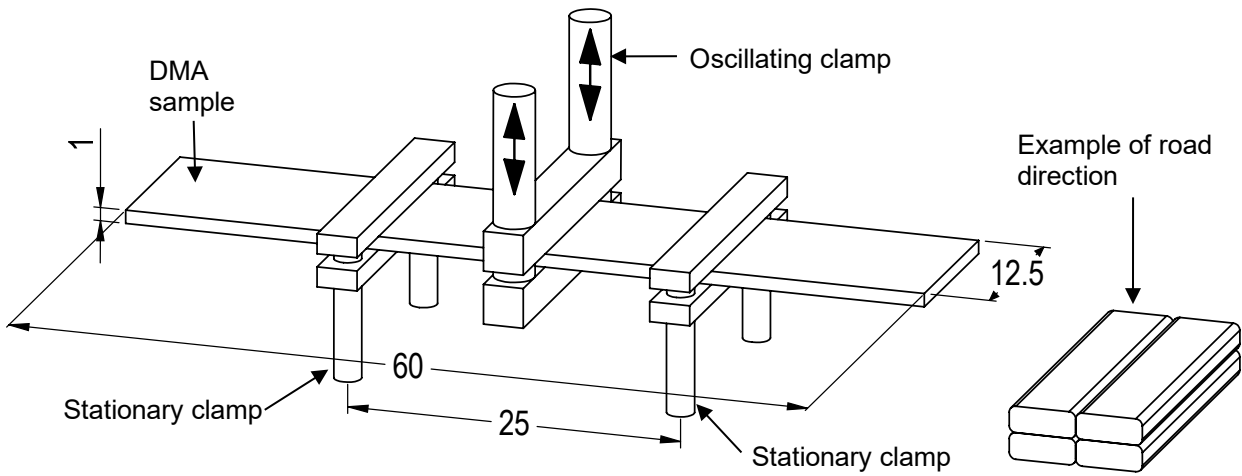


Figure 8: The relative position of the DMA sample to the clamping setup and the print direction

3.2.5 Creep samples

The creep experiments according to ASTM D2990 required rectangular $60 \times 12.5 \times 3$ mm bar-shaped samples. The position of the sample relative to the road direction is illustrated in Figure 9. The samples were printed using the same print parameters and machining process utilised in the creation of the instantaneous tensile samples. A total of 36 samples were produced, 18 samples for the temperature creep experiments and 18 samples for the ageing creep experiments. There was no difference in the samples required for the temperature and ageing creep experiments.

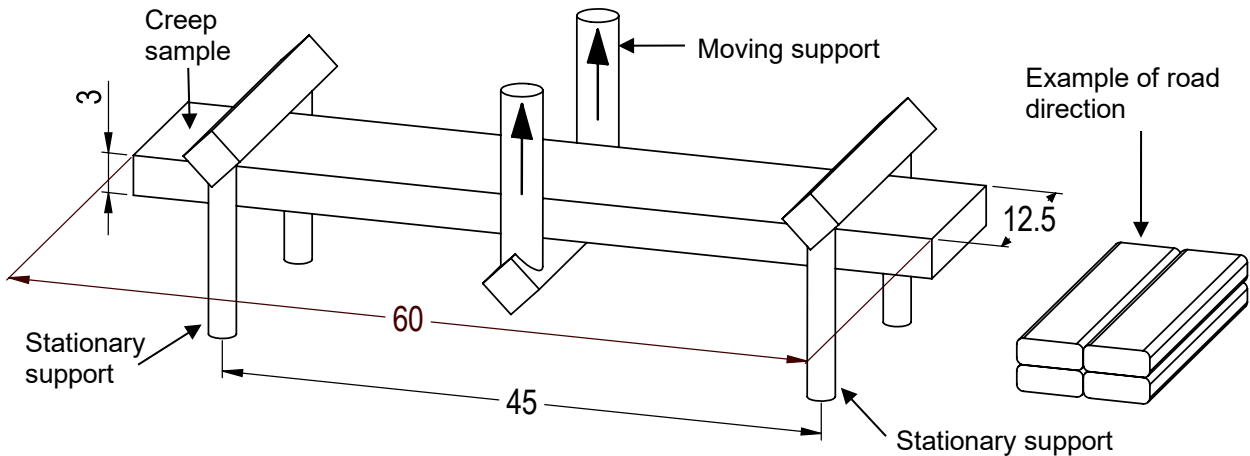


Figure 9: The relative position of the creep sample to support setup and the print direction

3.2.6 Sample overview

An overview all samples and their used within this article is provided by Table 3.

Sample Designation	Sample dimensions	Number of samples	Experiment designation
Tensile samples	25×250×3 mm	8	E ₁ , E ₂ , E ₃ experiments.
Tensile samples	25×250×3 mm	4	G ₁₂ , G ₁₃ , G ₂₃ experiments
E ₂ tensile sample	25×250×3 mm	1 (8 roads)	Road dimension experiments
E ₂ and E ₃ tensile sample	25×30×3 mm	2	Density experiments
DMA samples	60×12.5×1 mm	4	DMA experiments
Creep samples	60×12.5×3 mm	18	Temperature creep experiments
Creep samples	60×12.5×3 mm	18	Aging creep experiments

Table 3: Sample overview

3.3 Experimental setup

3.3.1 Ageing clock reset procedure

Preceding the experiments, the ageing clock of each sample was reset using the heat treatment process. A reset temperature of 20 °C above the material's T_g was selected, in line with Pierik et al. [20]. An oven was thus preheated to a temperature 100 °C, with 2 aluminium plates and four 1 mm or 3 mm aluminium shims, as shown in Figure 10.

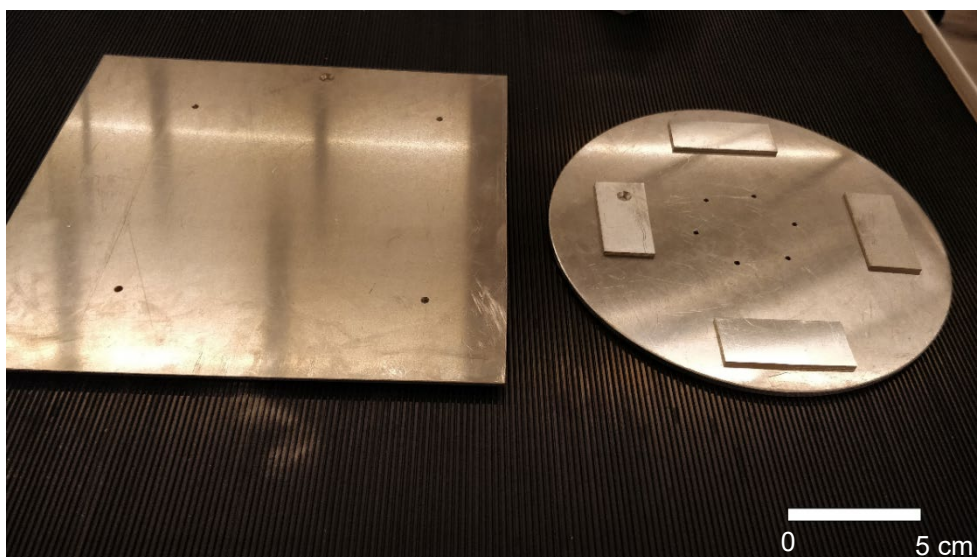


Figure 10: Heating plates and four shims

Once the oven had finished preheating, the samples were placed on the circular plate around the shims. The square plate was subsequently placed over the samples resting on the shims. The samples in this stack were not compressed but were restricted enough to prevent heat induced deformation. This stack was left in the oven for 10 minutes and subsequently removed to cool down. The age of a sample was measured from this point onwards. The age of all samples was reset before testing, ensuring all samples had the same age, to future reduce any sample variation and improve the samples' quality.

3.3.2 Tensile test experiments

The tensile tests were performed on a Shimadzu AGS-50KNXD Universal Tester equipped with self-aligning grips, which recorded the force and displacement in the longitudinal direction of the sample. The strain rate was set to 2 mm/min with a data capture rate of 20 Hz. All tests were performed in a standard laboratory with a temperature of 23 °C (± 2 °C) and a relative humidity of 50 % (± 5 %). The experimental setup is shown in Figure 11.

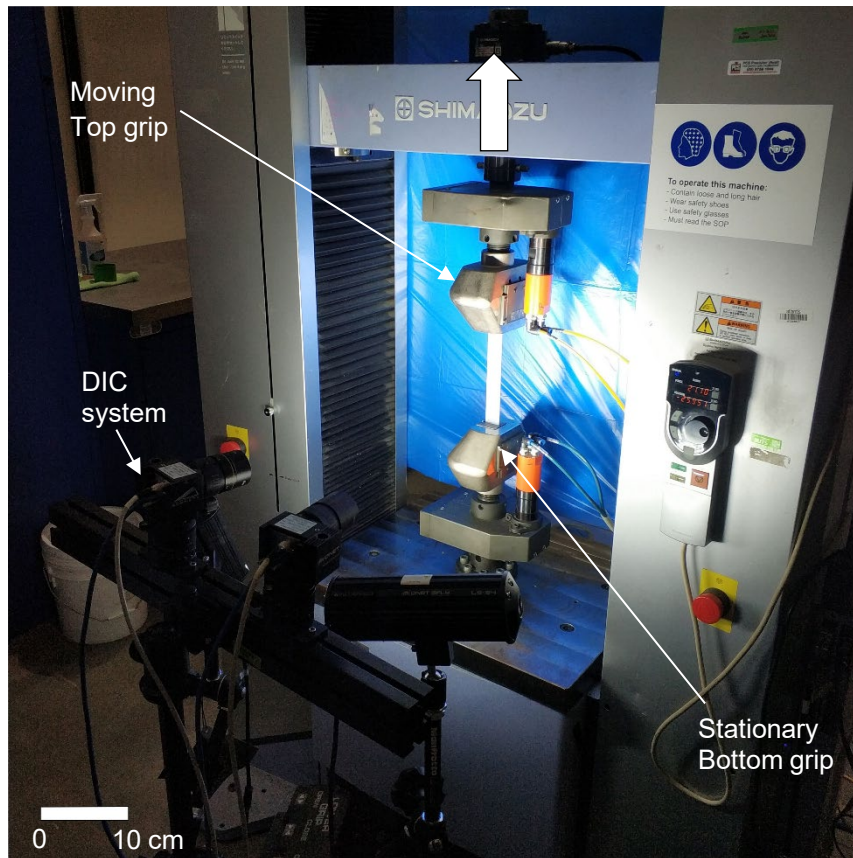


Figure 11: The tensile test experimental setup

The longitudinal and transverse in-plane displacement were captured using the Monet 3D Digital Image Correlation (DIC) system equipped with two MONET-3D-5U camera's each having a resolution of 5 MPx and a sampling rate of 50Hz. The cameras were fitted with 35 mm focal length lenses and positioned approximately 1 m away from the sample, well within the 280-2800 mm working distance of the cameras. The DIC system was set up so that the largest side of the sample faced the DIC. Three sets of two points, each spaced roughly 80 mm apart, were digitally selected on the sample's face in the DIC software, to allow three virtual vertical lines to be used for the longitudinal in-plane displacement measurements. The same process was followed to create 3 virtual horizontal lines of roughly 20 mm length for the transverse in-plane displacement measurements.

Before testing, the ageing clock of test sample was reset using the procedure described in section 3.3.1. After resetting the ageing clock, each sample's cross-sectional dimensions were measured at three locations between the tabs to three significant figures. Samples were ensured to have reached a temperature and humidity equilibrium before testing commenced and 8 samples were tested to failure for each direction in the E_1 , E_2 , E_3 and 4 samples in the G_{12} , G_{13} , G_{23} experiments.

3.3.3 Road dimensions experiments

To determine a representative unit cell of the printed material, microscopic scans were performed on the E_2 samples using an Olympus OLS5000 3D laser scanning confocal microscope. A 15 mm \times 15 mm scan area was selected on the largest face of the E_2 sample, away from the fracture location and tabs, using a 10 \times zoom factor.

3.3.4 Density experiments

The density of the additively manufactured material was measured using a Kern ANS-N analytical balance with accompanying KERN YDB-03 universal density determination set. A sample was weighed in air, subsequently submerged and weighed again, where care was taken to exclude air entrainment. The balance system calculated the density of the sample based on the two measurements.

As the E_3 samples were cut to avoid intersection with the voids, as illustrated in Figure 2, such a sample allowed the density of the feedstock to be determined. On the other hand, the E_2 samples are positioned perpendicular to the void direction, thereby cutting through several voids and its density is thus that of the extruded material.

3.3.5 DMA experiments

The DMA experiments were performed on a PerkinElmer DMA 8000 Analyzer using a dual cantilever clamping method, where an oscillating clamp is centred between two stationary clamps spaced 45 mm apart, as illustrated in Figure 8. During the strain sweep the amplitude of the moving clamp was increased from 0.001 mm to 1 mm at a fixed frequency of 10 Hz. Each of the 4 samples experienced this strain sweep ten times and the results were averaged over the ten cycles. The DMA 8000 was equipped with a temperature-controlled chamber to perform the DMA experiments at 75°C.

Before testing, the cross-sectional dimensions of each sample were measured, using a digital vernier calliper, to two significant figures and entered into the analyser's software. Care was taken to reset the ageing clock of the samples before testing. The DMA analyser logged the displacement of, and the force exerted on the oscillating clamp. These measurements are combined with the cross-sectional dimensions of the sample to calculate the progression of the storage modulus versus the strain of each sample.

3.3.6 Temperature creep experiments

A bespoke creep setup, shown in Figure 12, compliant with the ASTM D2990 standard, was used for the temperature creep experiments. The samples were loaded in three-point bending by an upwards-moving roller centred between two stationary support rollers spaced 45 mm apart, as shown in Figure 9 and Figure 13.

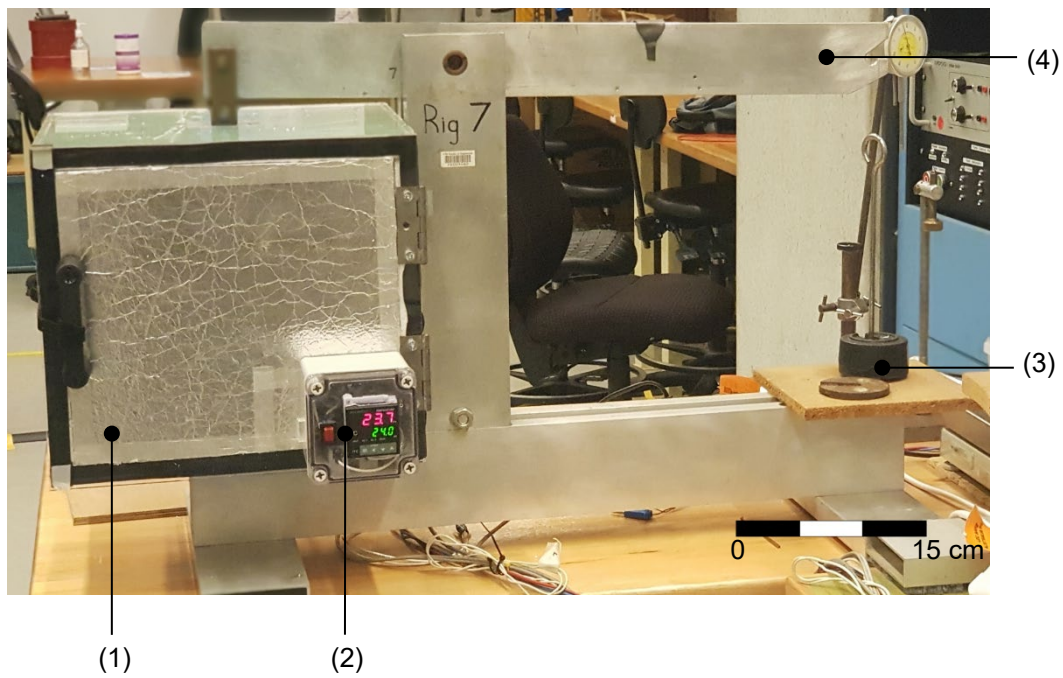


Figure 12: External view of the creep rig configuration. (1) Temperature-controlled chamber. (2) Temperature control unit. (3) Disc weights. (4) Lever arm [26]

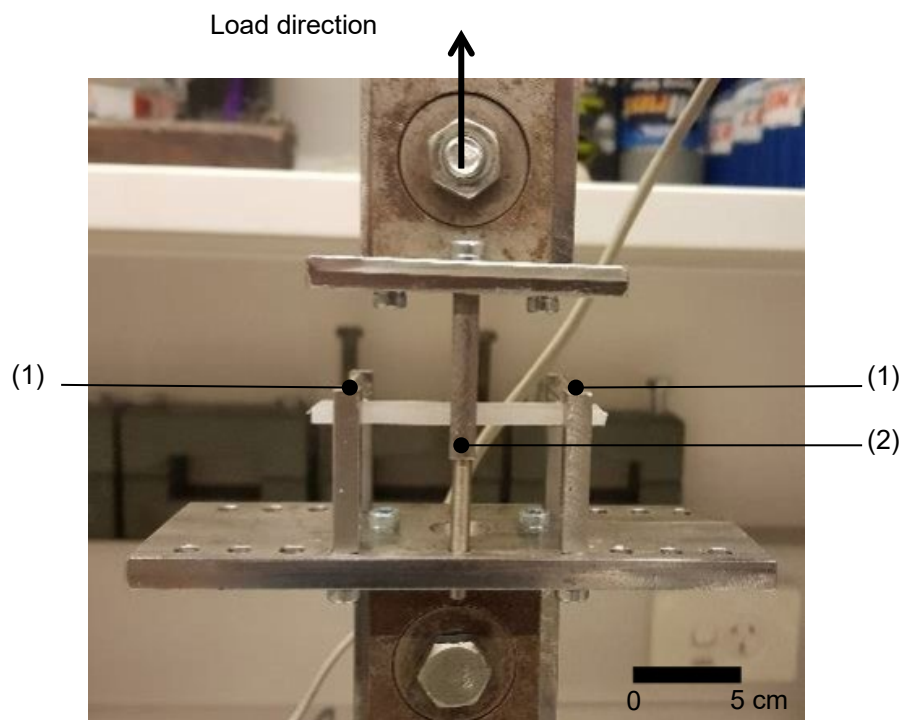


Figure 13: Internal view of the creep rig configuration. (1) Support roller. (2) Moving loading roller [26]

The DMA experiments found that a load of 1 kg signals the end of the LVR. Since the offset hinge point of the lever arm doubled the load on the sample compared with the disc weight, a 0.5 kg disc weight was applied, smoothly and within 5 s. The vertical displacement of the arm was recorded using a computer-connected NI 9205 data acquisition module at 3 Hz via the LabView software package. An environmental chamber surrounded the creep sample and allowed the test temperatures to be set.

Three samples were tested at each of the following temperatures (± 2 °C): 23 °C, 45 °C, 55 °C, 60 °C, 65 °C, and 70 °C, all at a relative humidity of 45 %. Prior to testing, samples were

conditioned at each test temperature for at least 48 h and each sample's cross-sectional dimensions were measured to three significant figures.

Using the ageing clock reset procedure, the age of the samples was reset, and the samples were left to age for 221 h before testing commenced. Adhering to the snap-shot assumption, this age allowed a creep test duration of 22.1 h.

The maximum fibre stress (in MPa) for each sample was calculated as,

$$\sigma = \frac{3Pl}{2wt^2} \quad (9)$$

Where σ is the Von Mises Stress, l is the span between the two stationary supports, w is the sample width, and t is the sample thickness. While the maximum strain in the outer-fibre at the mid-span was calculated as,

$$\varepsilon = \frac{6yh}{l^2} \quad (10)$$

Where ε is the maximum strain, y is the maximum deflection at mid-span, h is the sample thickness, and l is the span between the two stationary supports. The creep compliance (D) was calculated by dividing the strain (ε) by the stress (σ) over time.

3.3.7 Ageing Creep experiments

The ageing creep experiments were performed using the same bespoke creep setup as the temperature creep experiments for the 1 kg load case. Since the creep results were converted into a log-log scale, it was preferred for the resulting graphs to be equidistantly spaced on this scale. This was achieved by ensuring the age of the samples aligned with the 10^x regime, similar to Barbero [19], multiplied by 24 h. This resulted in the sample ages listed in the second column of Table 4, including an older sample, aged for 221 h.

Ageing Creep Test Designation	Age of the sample	Creep test duration
14 min	0.24 h (24×10^{-2}) = 14 min	0.024 h = 1 min: 26 s
46 min	0.76 h ($24 \times 10^{-1.5}$) = 46 min	0.076 h = 4 min: 33 s
2 h:24 min	2.4 h (24×10^{-1}) = 2 h: 24 min	0.24 h = 14 min: 24 s
7 h:35 min	7.59 h ($24 \times 10^{-0.5}$) = 7 h: 35 min	0.76 h = 45 min: 32 s
24 h	24 h (24×10^0) = 1 d	2.4 h = 2 h: 24 min
221 h	221 h = 9 d: 5 h	22.1 h = 22 h: 6 min

Table 4: Ageing creep experiment overview

Adhering to the snap-shot assumption, the duration of each of these 6 ageing creep experiments are listed in the last column of Table 4. Three samples were tested for each of the 6 ages and the results have been averaged for each age group. All ageing creep experiments are performed at 45 °C (± 2 °C) and 45 % relative humidity. Prior to testing, samples were conditioned at 45 °C for at least 48 h and each sample's cross-sectional dimensions were measured to three significant figures. The creep compliance values can then be calculated in the same way as was done in the temperature creep experiments.

4 Results and discussion

The results of the tensile, DMA, temperature creep, and ageing creep experiments are discussed in this section. The creation of the master curve using the experimental results is also described.

4.1 Tensile experiments (Instantaneous mechanical properties)

The E_1 , E_2 , E_3 experiments resulted in data sets of tensile force versus vertical displacement, measured by the universal tensile tester, and the longitudinal and transverse displacement of points on the sample surfaces, measured by the DIC system. The results were aligned using the points of failure in the data sets as a reference point. The longitudinal displacement along three lines were averaged and the same approach was applied to the transverse displacement. The averaged stress and strain at each data point was calculated as specified in the ASTM D3039 standard and graphed. This allowed a stress-strain curve to be plotted for each sample. Linear regression was conducted in the range of strain 0.002 – 0.004 to acquire the Young's modulus for each sample. The Young's modulus of each of the five samples were averaged per material direction and the results, including the CoV, the dispersion of data point around their mean utilised by other researchers [19, 20], are given in Table 5.

Material constant	Young's Modulus (MPa)	CoV (%)
E_1	1898.7	2.98
E_2	1272.4	28.07
E_3	1894.8	3.07

Table 5: Young's moduli resulting from the E_1 , E_2 , E_3 experiments

Two additional trendlines were fitted to the results to longitudinal and transverse strain data between 0.003 and 0.005 of strain. Dividing the coefficient of the transverse trendline with that of the longitudinal trendline produced a Poisson's ratio per sample. The five samples were averaged resulting in the Poisson's ratio per material direction, as given in Table 6.

Material constant	Poisson's ratio	CoV (%)
ν_{12}	4.01×10^{-1}	4.60
ν_{23}	3.73×10^{-1}	23.77
ν_{13}	4.61×10^{-1}	11.91

Table 6: Poisson's ratios resulting from the E_1 , E_2 , E_3 experiments

The same approach to calculate the Young's modulus was applied to the G_{12} , G_{13} , G_{23} experiments resulting in the very similar off-angle moduli, as listed in Table 7.

Off-angle constant	Young's Modulus (MPa)	CoV (%)
$E_{12_45^\circ}$	1797.6	1.80
$E_{23_45^\circ}$	1829.3	2.38
$E_{13_45^\circ}$	1816.2	3.52

Table 7: Off-angle Young's moduli resulting from the G_{12} , G_{13} , G_{23} experiments

The results listed in Table 5, Table 6 and Table 7 were entered into Eq. (2), Eq. (3) and Eq. (4) to calculate the shear moduli and their coefficients of variation, as listed in Table 8.

Material constant	Shear Modulus (MPa)
G_{12}	748.8
G_{23}	685.5
G_{13}	611.7

Table 8: The calculated shear moduli

Again, two roughly equal shear moduli were found in two directions accompanied by a lower value in the shear direction 13.

4.1.1 Road dimensions experiments

The commercial Solidworks software suite was used to trace the outline of 18 voids, using semicircular elements, in the microscopic scan of the largest face of an E_2 sample, shown as red

solid lines in Figure 14. These voids surround the cross-section of 10 roads, illustrated by the red dashed lines in Figure 14.

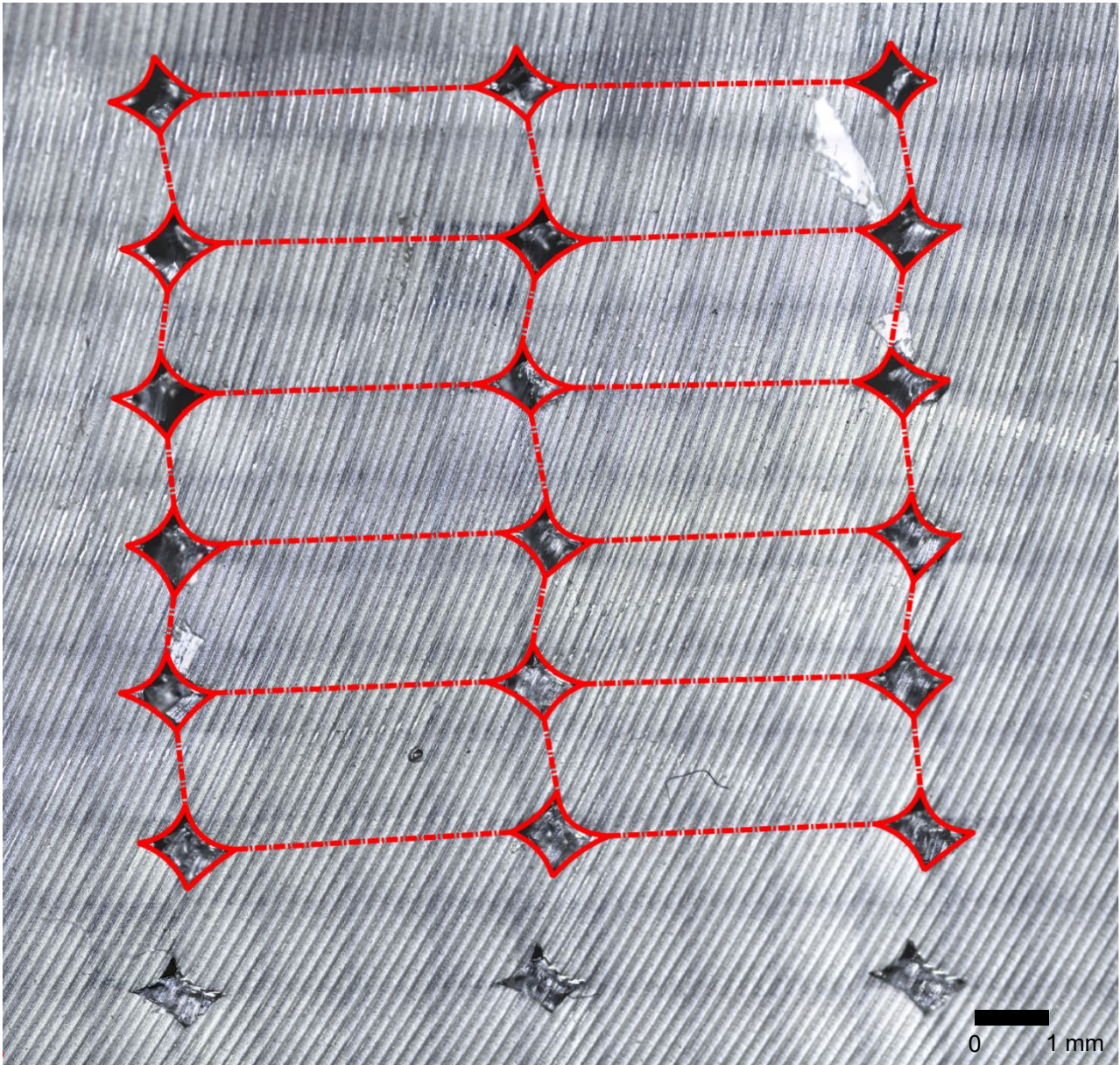


Figure 14: Traced cross-sectional shape of the printed roads

The diagonal lines in Figure 14 are caused by the milling step during the sample's preparation where the spacing between the lines testifies to the small passes of this machining step. A slight tilt of the roads can be observed in Figure 14 which was caused by the misalignment of the sample relative to the microscope in the plane of view. The tilt angle to the horizontal was measured for each dashed line, averaged and used to level the roads. The start points, end points and radius of every semicircular element was extracted and averaged to derive a representative cross-sectional shape of the printed material, as shown in Figure 15.

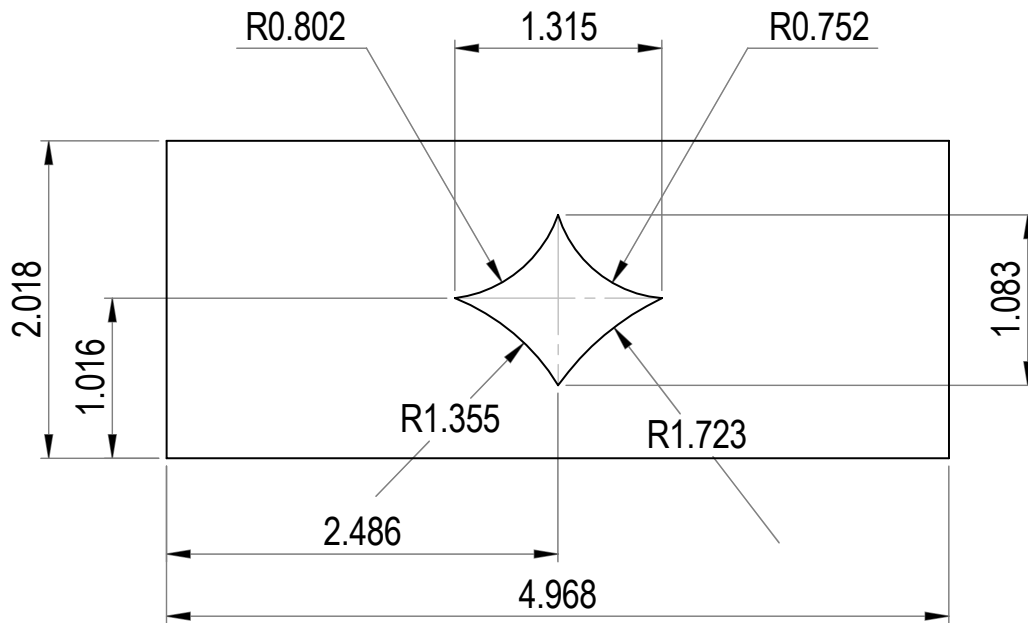


Figure 15: Averaged cross-sectional shape of the printed road

The representative road cross-sectional shape shows that the void location is roughly halfway along the width and height of the road. Furthermore, the void shape is slightly wider than it is high and the radii of the bottom quadrants of the void are larger than those of the upper quadrants, indicating that the bottom corners of the deposited roads curve more than the top corners.

This averaged road was then extruded by 10 mm to form a unit cell which was analysed using the commercial Ansys Material Designer software suite, as used by other researchers to extract homogenised material properties [48-50]. A view of the unit cell, with meshing applied, is shown in Figure 16.

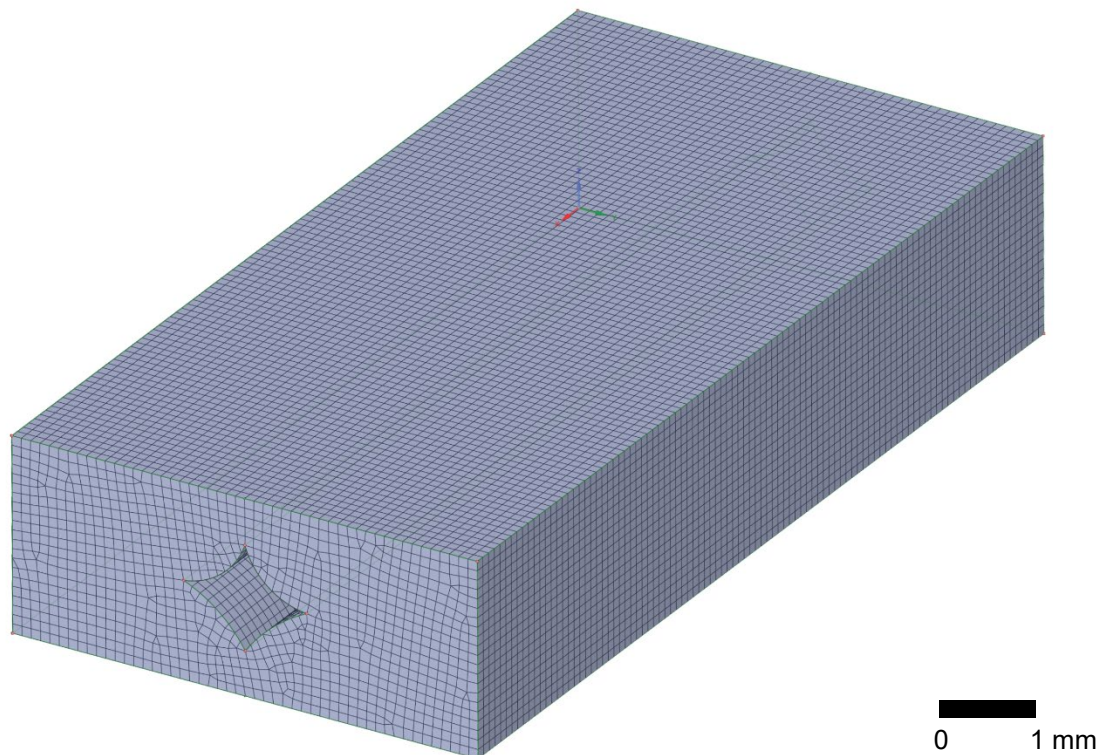


Figure 16: The meshed unit cell of the printed road

A Young's modulus of 2308 MPa of the SKYGREEN® S2008 feedstock, as measured by Hadiouch et al. [51], was inputted into the software. The analysis resulted in the Young's moduli of the printed unit cell, as listed in Table 9.

Material constant	Young's Modulus (MPa)
E ₁	2193.9
E ₂	1929.0
E ₃	1912.9

Table 9: Young's moduli resulting from the unit cell experiments

The unit cell represents a theoretical version of the printed material which is absent of any adhesion problems or print errors. The Young's moduli in Table 9 thus form the upper theoretical limit of these properties. When the theoretical results of Table 9 are compared to the experimentally obtained values of Table 5, several differences become apparent.

The E₁ samples have their roads aligned with the direction of the tensile force and these continuous roads are expected to result in a high Young's modulus in this direction. While the E₁ modulus is indeed the highest of the theoretical results by far, the experimental E₁ Young's modulus is nearly equal to that in the E₃ direction. The theoretical and experimental Young's modulus values in the E₃ direction are within 1% of each other but the experimental Young's modulus in the E₁ direction is only 86.5% of the maximum achievable value. A possible explanation for the deficiency in the E₁ direction are print errors, inherent to the extrusion-based additive manufacturing process.

Finally, a comparison between the theoretical and experimental values of the Young's modulus in the E₂ reveals that the experimental value is only 66.0% of the theoretically achievable value. A possible explanation is the poor inter-road adhesion in this direction as the adhesion is only achieved by the slight pressure the settling road exerts onto the road in place. This width-wise compression is likely to be small compared to the effect of the gravitational force on the contact area in the E₃ direction, leading to possible poor adhesion. Further supporting this poor width-wise adhesion theory is the high CoV value in the E₂ direction.

4.1.2 Density experiments

The results of the density experiments were as follows. The density of the feedstock was found to be 1292.6 kg/m³ and the measured value of the extruded material was 1274.2 kg/m³. The lower density of the extruded material is testament to the inherent void creation during the additive manufacturing process.

4.2 DMA experiments

The results from the DMA experiments are shown in Figure 17, where the storage modulus is plotted versus the displacement on the moving clamp.

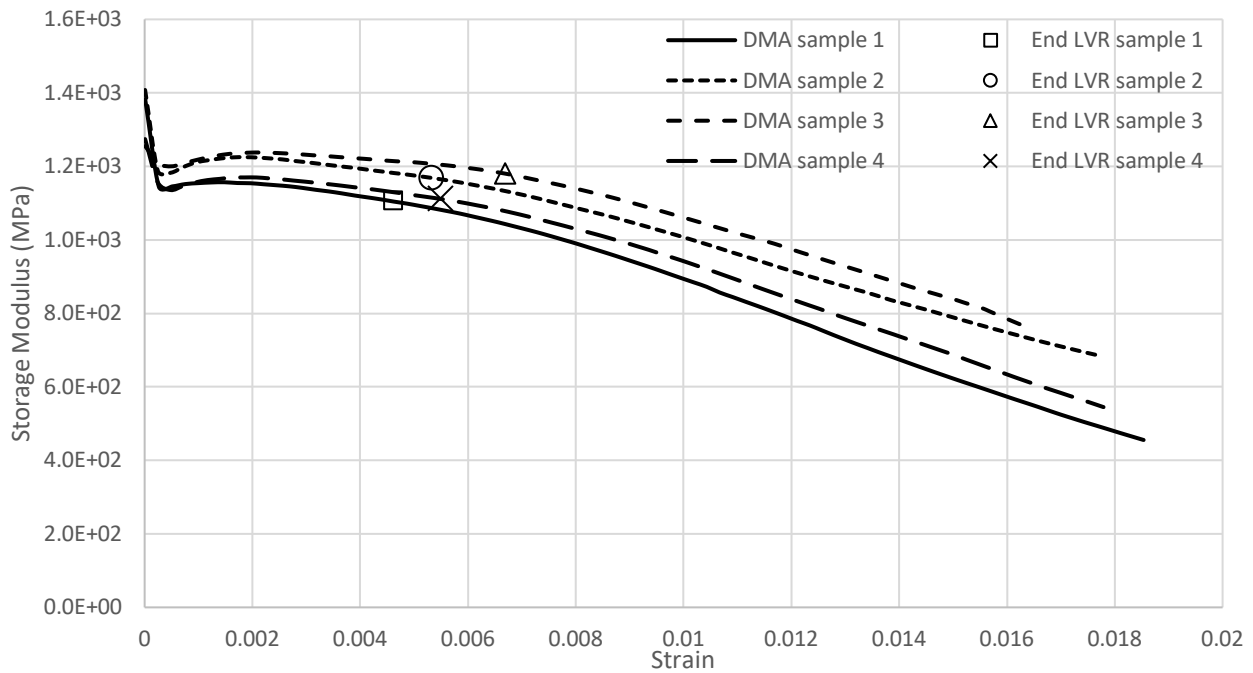


Figure 17: The storage modulus vs strain results of the DMA experiments

Initially, a rapid change in the storage moduli can be seen which is believed to be the settling of the samples in the clamp. The storage moduli plateau soon after. The point where the modulus drops 5% below its highest value on this plateau marks the end of the linear viscoelastic range (LVR). These points are highlighted in Figure 17 and listed in the second column of Table 10, including their average and the coefficient of variation.

DMA Test Designation	End of the LVR: Storage Modulus (MPa)	End of the LVR: Stress (MPa)	End of the LVR: Load (kg)
DMA Sample 1	1.10×10^3	5.32	0.90
DMA Sample 2	1.16×10^3	6.43	1.09
DMA Sample 3	1.18×10^3	8.03	1.36
DMA Sample 4	1.11×10^3	6.08	1.03
Average	1.14×10^3	6.46	1.09
CoV	2.96 %	15.25 %	15.25 %

Table 10: DMA results

The DMA experiments were conducted using the dual cantilever clamping method for 1 mm thick samples, whereas the creep experiments used a 3 mm thick sample and a three-point bending support method. A conversion step is required to transform the stress results from the DMA experiments, listed in the third column of Table 10, to an applied force in the creep experiments.

The DMA software applies a strain factor and geometry factor in the calculation of the strain and stress response of the sample which differs between a dual cantilever and three-point bending clamp method. These factors are given in Table 11, where l is half the distance between stationary supports, t is the sample thickness, and w is the sample width.

Clamping method	Geometry Factor	Strain Factor
Dual Cantilever	$2w \left(\frac{t}{l}\right)^3 / \left(1 + 2.9 \left(\frac{t}{l}\right)^2\right)$	$\frac{3t}{l^2}$
Three-point Bending	$\frac{w}{2} \cdot \left(\frac{t}{l}\right)^3$	$\frac{3t}{2l^2}$

Table 11: The Geometry and Strain factors for the dual cantilever and three-point bending clamping methods

The Von Mises stress in the sample is calculated by the software. When this variable is multiplied by the geometry factor over the strain factor, the force on the sample can be calculated. The Von Mises stress from the dual cantilever DMA experiments are thus multiplied by the three-point bending geometry factor over the strain factor to produce the force at the end of the LVR for a three-point bending experiment. The resulting forces are listed in the last column of Table 10 and mark the end of the LVR for the creep samples used in the temperature and ageing creep experiments. The average over all four samples is 1.09 kg, which was rounded down to remain within the LVR. A load of 1 kg was thus applied in the temperature and ageing creep experiments.

4.3 Temperature creep experiments

The creep experiments at the two highest temperature, 65 °C and 70°C, were not successful as two of the three samples broke in the former, and all samples broke in the latter, before the end of the 22.1 h creep test duration. While the creep behaviour of the 65 °C samples was acceptable until 11 h, all 70 °C samples failed after 16 min. The creep response of the 65 °C samples up to 11 h was therefore considered while the 70 °C creep results were discarded.

Since the recording of the sample's deflection was started before the creep load application, the time scale of creep deformation response of three samples were aligned by the point of load application. Using each sample's dimensions, the sample's strain and stress were calculated and combined into the creep compliance for each sample. The creep compliance was then averaged over the three samples for each temperature and this average was approximated by a power law, as was applied by other researchers [19, 52, 53]:

$$D(\lambda) = D_0 + D_1\lambda^m \quad (11)$$

Where λ is the time elapsed since the load application, $D(\lambda)$ is the creep compliance since the load application, D_0 is the elastic compliance, D_1 a compliance coefficient, and m is the power constant.

Figure 18 shows an example of the outcome of these steps: the average creep compliance for the creep experiment at 23 °C, including the deviation from the average along the curve. Also visible in Figure 18 is the excellent power law fit with a correlation coefficient of 0.9895.

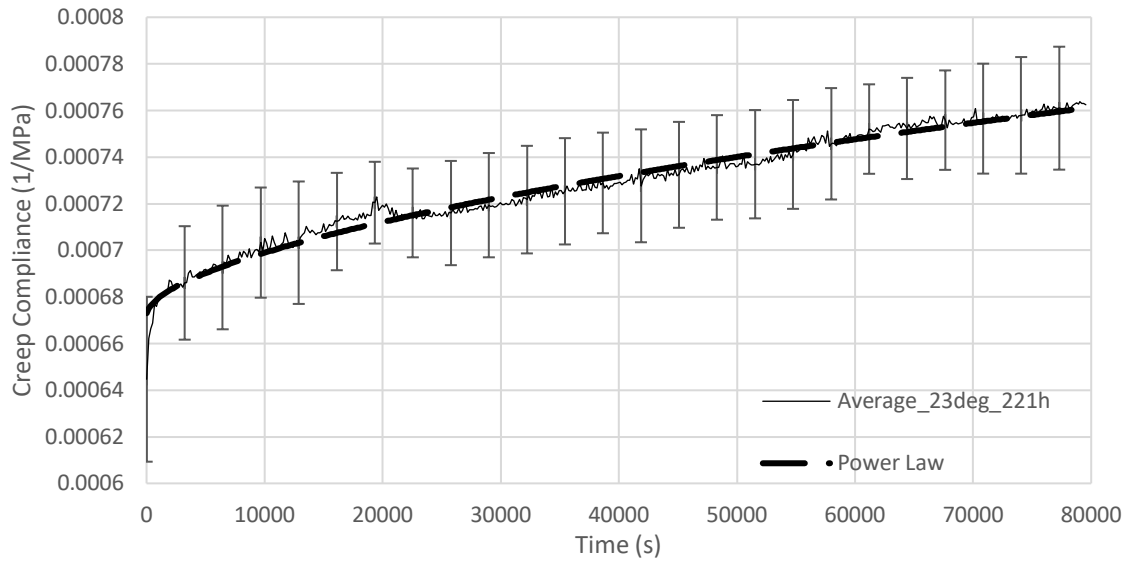


Figure 18: The average creep compliance and power law curve fit for the 23 °C temperature creep experiment

The power law curves of the creep behaviour at 23 °C, 45 °C, 55 °C, 60 °C and 65 °C are shown in log time as dashed lines in Figure 19.

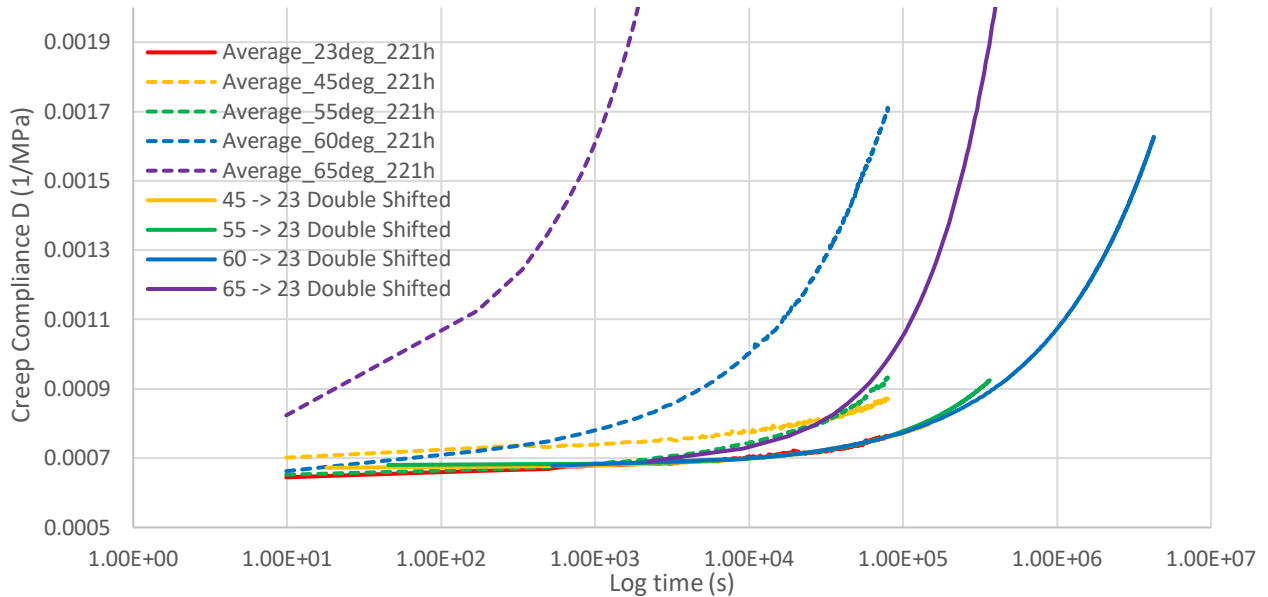


Figure 19: The power law creep compliance curves for the temperature creep experiments

The compliance coefficients of the power law curve fits of the experiments are listed in column 2, 3 and 4 of Table 12.

Temp. test designation	D_0	D_1	m	$a(T)$	$b(T)$
23 °C	6.73×10^{-4}	1.24×10^{-7}	5.82×10^{-1}	1	1
45 °C	7.33×10^{-4}	2.31×10^{-7}	5.66×10^{-1}	1.8251	1.0913
55 °C	6.83×10^{-4}	8.12×10^{-8}	7.10×10^{-1}	4.5921	1.0044
60 °C	7.10×10^{-4}	1.15×10^{-6}	6.00×10^{-1}	53.3928	1.0532
65 °C	1.32×10^{-3}	6.44×10^{-7}	9.28×10^{-1}	Excluded	
70 °C			Excluded		
Momentary master curve	6.68×10^{-4}	1.49×10^{-7}	5.74×10^{-1}		

Table 12: Regression parameters and shift factors for the temperature creep experiments

To create the master curve, the power law approximations at higher temperatures needed to be shifted both horizontally and vertically to superimpose on the power law curves of a lower temperature creep response. To shift a creep curve horizontally, the creep compliance values at a temperature T in time scale λ , defined as $D(\lambda, T)$, needed to be plotted against a modified timescale [19, 54]. To achieve this, the time scale λ was multiplied by a so-called 'horizontal shift factor', $a(T)$, resulting in the same creep compliance values but as a function of the modified timescale: $D(a_T \lambda, T)$. For instance, to apply the 45 °C curve fit to the 23 °C data points, λ_{45} in the curve fit was to be modified by $a(T)$ to align with the λ_{23} data set, according to $\lambda_{23} = a(T) \times \lambda_{45}$. A vertical shift could be accomplished by applying a correction factor, the 'vertical shift factor', $b(T)$, to the creep compliance values themselves. Thus, if the creep compliance curve at temperature T could be superimposed on the curve at another temperature T_r , the following applies,

$$D(\lambda, T) = \frac{D(a_T \lambda, T_r)}{b_T} \quad (12)$$

In this research, the master curve was created at a reference temperature of 23 °C so the other power law approximations were shifted horizontally and vertically onto the 23 °C data points. As an example, shifting the power law approximation of the 45 °C data set horizontally and vertically onto the 23 °C data points requires Eq. (11), using the regression parameters of the 45 °C data: $D_{0;45}$ and $D_{1;45}$ and m_{45} , to be combined with Eq. (12) for $T = 23$ °C to form,

$$D(\lambda_{23}, 23) = \frac{\left(D_{0;45} + D_{1;45} \left(\frac{\lambda_{23}}{a_T} \right)^{m_{45}} \right)}{b_T} \quad (13)$$

When using the D_0 , D_1 and m regression coefficients from Table 12, the shift factors $a(T)$ and $b(T)$ could then be calculated by fitting the remaining temperature power laws to the 23 °C data points. The resulting shift factors per temperature are listed in the last two columns of Table 12 and the shifted curves are shown as solid lines in Figure 19.

It is clear from Figure 19 that the creep response for the 65 °C experiments did not superimpose into a smooth master curve like the curves at the other temperatures. Combined with the fact that the total duration of the creep experiment could not be achieved at this temperature, the 65 °C results were excluded from further steps towards the creation of a master curve.

The superposition of the remaining creep curves results in a so-called 'momentary' master curve since the input creep experiments excluded the effects of ageing. This momentary master curve could be approximated by a power law with the coefficients $D_0 = 6.68 \times 10^{-4}$, $D_1 = 1.49 \times 10^{-7}$ and $m = 5.74 \times 10^{-1}$, as given in the last row of Table 12. The combined momentary master curve in

Figure 19 ends at 4.21×10^6 s, or 49.15 days, which given the 22.1 h duration of the creep experiments, clearly shows the benefits of the creep prediction process. Since ageing dampens the compliance increase of the master curve, the creep duration of the master curve will be further extended.

While the shift factors, $a(T)$ and $b(T)$, in Table 12 were calculated for the experimental temperatures, an interpolation of the shift factor values outside of these temperatures would allow the creation of a master curve at any desired temperature. Such an interpolation is achieved by applying Williams-Landel-Ferry (WLF) equation [55] applied to the log values of $a(T)$ as follows,

$$\log a_T = \frac{C_1(T - T_r)}{C_2 + T - T_r} \quad (14)$$

The same formula was applied to the log values of $b(T)$. The resulting WLF curve fits to the measured shift factors, $a(T)$ and $b(T)$, are shown in Figure 20.

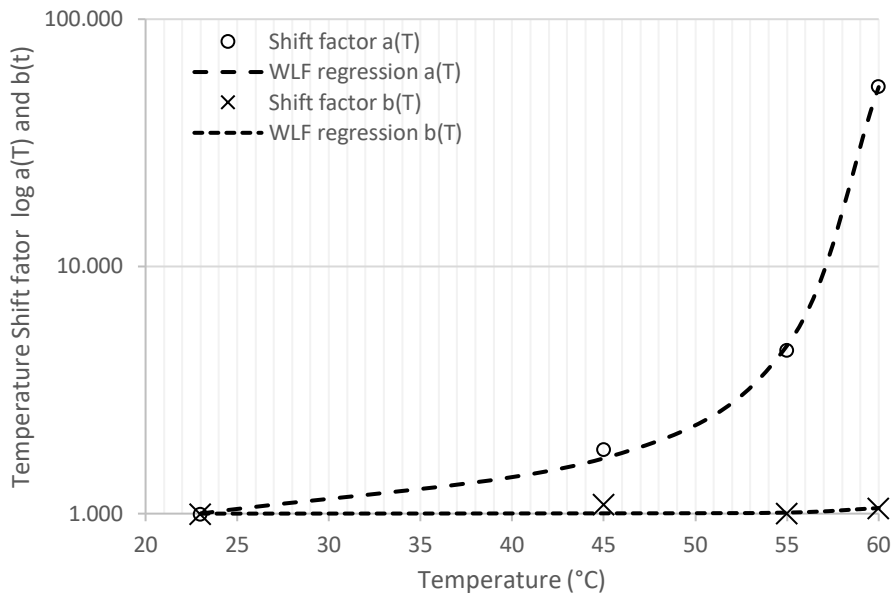


Figure 20: Temperature shift factors $a(T)$ and $b(T)$ and the WLF curve fits

The WLF curve of $a(T)$ shows a good fit, but the fit of $b(T)$ is not as good, especially around 45 °C. While $b(T)$ is generally less influential than $a(T)$ [56] and remains close to unity [57], other researcher have found no clear pattern in the vertical shift factor [58]. Thus, due to the poor regression of the vertical shift factor $b(T)$, care should be taken when creating the master curve for values besides the experimentally tested temperatures.

4.4 Ageing creep experiments

The same steps used in the creation of power law curve fits for different temperatures was applied to the creep behaviour of samples of different ages. The resulting power law curves of the aged samples are shown in log time as dashed lines in Figure 21.

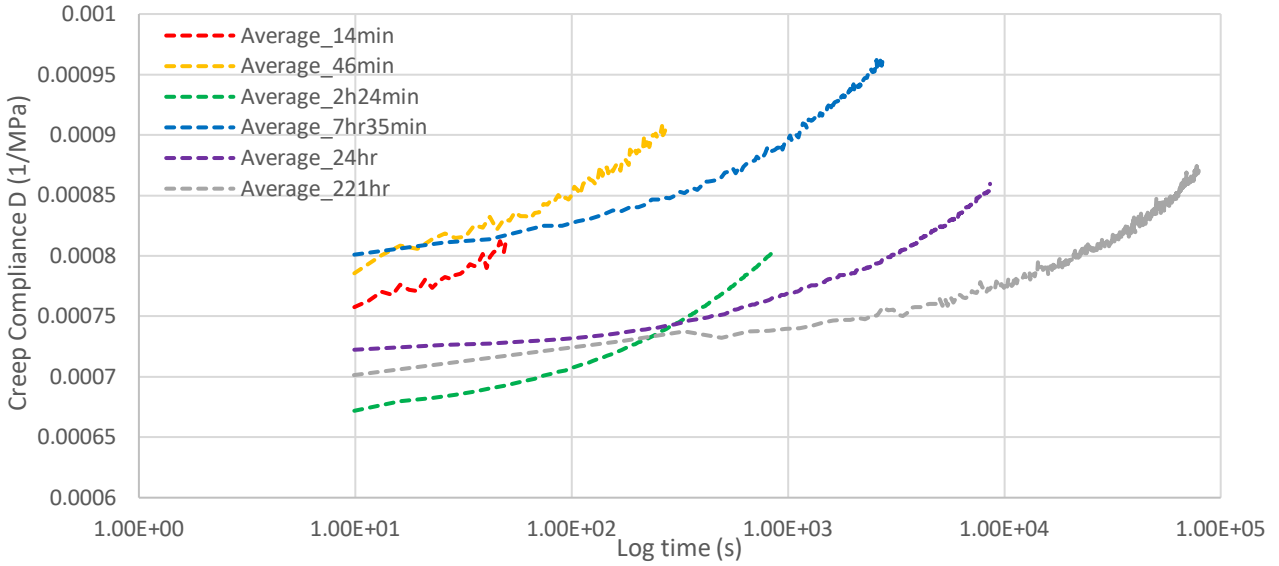


Figure 21: The power law creep compliance curves for the aged creep experiments

The compliance coefficients of the power law curve fits are listed in column 2, 3 and 4 of Table 13, including their average and the coefficient of variation.

Ageing Creep Test Designation	D_0	D_1	m	a_e
14 min	7.38×10^{-4}	4.58×10^{-6}	6.94×10^{-1}	6.42×10^2
46 min	7.69×10^{-4}	9.16×10^{-6}	4.82×10^{-1}	2.51×10^2
2 h:24 min	6.59×10^{-4}	4.48×10^{-6}	5.14×10^{-1}	9.45×10^1
7 h:35 min	8.00×10^{-4}	2.51×10^{-6}	5.27×10^{-1}	3.79×10^1
24 h	7.23×10^{-4}	1.20×10^{-6}	5.19×10^{-1}	8.10×10^0
221 h	7.33×10^{-4}	2.31×10^{-7}	5.66×10^{-1}	1×10^0
Average	7.37×10^{-4}	3.69×10^{-6}	5.50×10^{-1}	
CoV	6.41 %	86.38 %	5.42 %	

Table 13: Regression parameters and shift factors for the ageing creep experiments

Barbero [19] showed that the elastic compliance D_0 is independent of age, which is supported by the low 6.2 % coefficient of variance in the average value of D_0 in Table 13, whereas D_1 is highly age dependent. When the power law from Eq. (11) is then reordered and log rules applied, the following equation formed,

$$\log(D(\lambda) - D_0) = \log D_1 + m \log \lambda \quad (15)$$

The ageing response curves were regressed again using the average m regression coefficient. Using this approximation, Eq. (15) then creates parallel data sets in a log-log graph, as shown as solid curves in Figure 22.

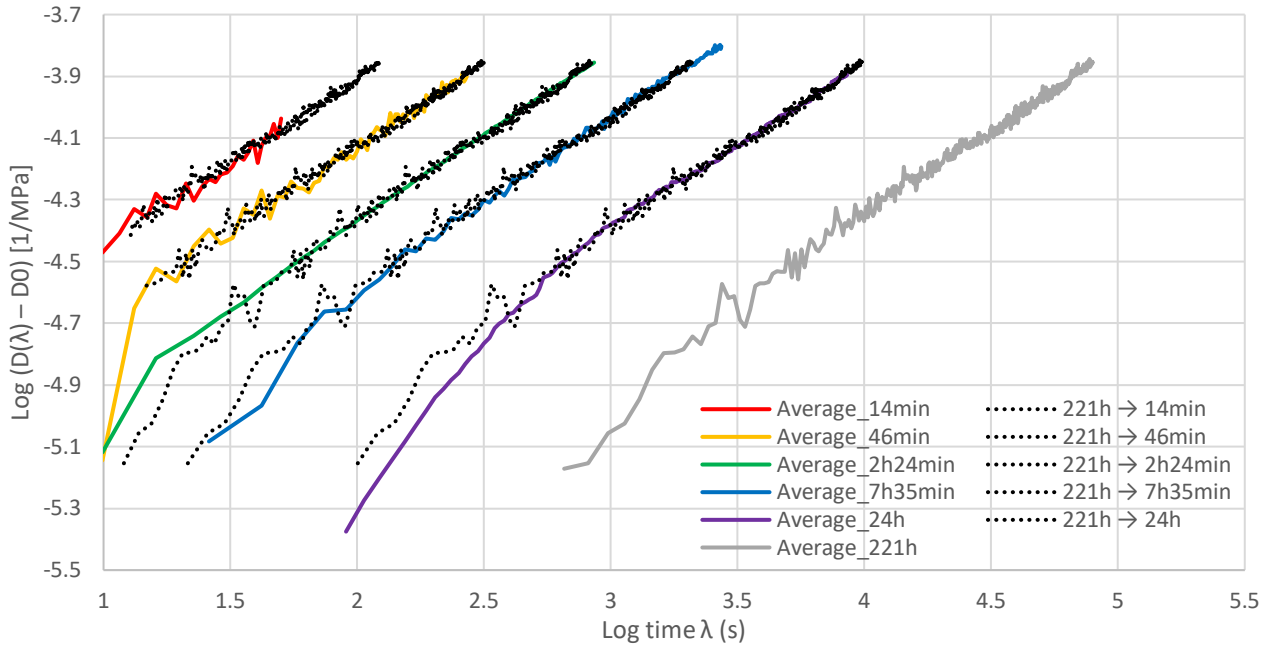


Figure 22: The modified power law fit of the ageing creep experiments

The horizontal distance between each curve is the log of the shift factor a_e , which is essential in the calculation of the ageing shift rate μ , when introducing the effects of ageing in the momentary master curve.

Since all curves have the same m values, they are superimposable. The horizontal distance a curve needs to be shifted to another curve is expressed as,

$$\log(D(\lambda) - D_0) = \log(D(a_e \lambda) - D_0) \quad (16)$$

Applying the log rules to Eq. (16) simplifies the equation to the following,

$$\left(\frac{D_1}{D_{1r}}\right)^{\frac{1}{m}} = a_e \quad (17)$$

The shift factors a_e when shifting the 221 h creep curve to lower age curves are given in the last column of Table 13. The results of shifting the 221 h creep curve by using the calculated shift factors are shown as black dotted lines in Figure 22 where excellent agreement with the creep data is evident.

A plot of the shift factors a_e versus ageing time t_e of the samples in log-log time then allows the extraction of the sought-after ageing shift rate, μ , as the coefficient of a linear trendline to the data point, as shown in Figure 23, using least squares regression. The ageing shift rate was calculated to be 0.9582 with an excellent R^2 value of 0.9941.

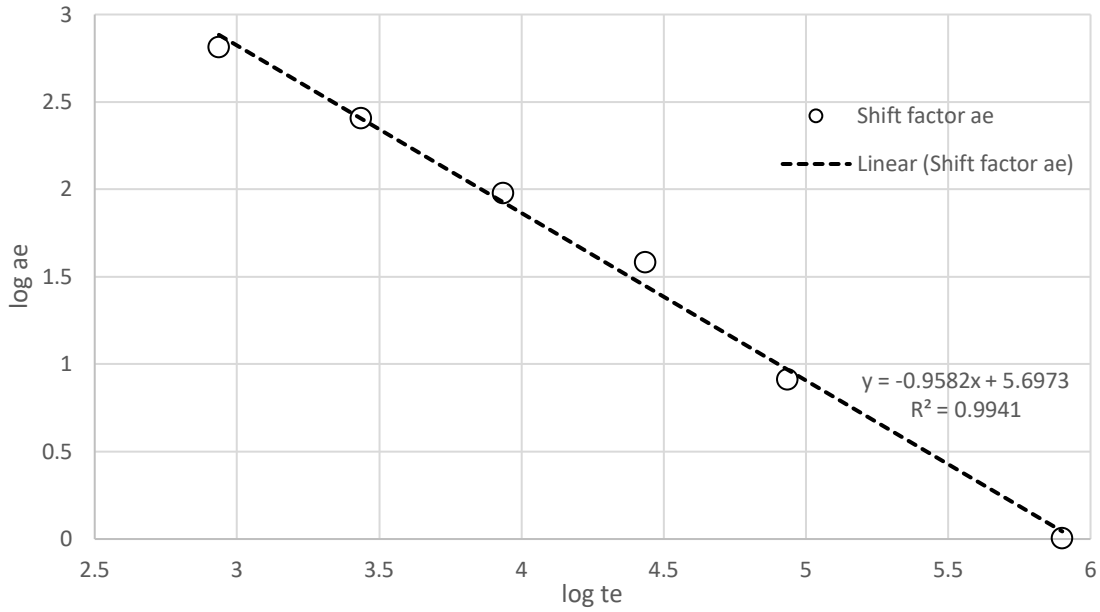


Figure 23: The shift factor versus ageing time in log-log scale

4.5 Master curve (Time-dependent material properties)

The ageing shift rate was utilised to introduce the effects of ageing into the momentary master curve to produce an age-affected prediction of the creep response of additively manufactured PETG. The effects of ageing were accounted for by modifying the time scale according to the so-called 'effective time' theory, which states that, for ageing shift rates smaller than 1, Eq. (18) applies.

$$\frac{t}{t_e} = -1 + \left(\frac{\alpha}{t_e} \lambda + 1 \right)^\alpha \quad (18)$$

Where t is the creep time, or duration of a creep experiment, t_e is the ageing time, or the age of the sample when the creep experiment commences, $\alpha = 1 - \mu$, μ is the ageing shift rate, and λ is the effective time.

When the Eq. (18) is applied to the momentary master curve, plotted for equidistantly spaced points in time, the creep prediction for a sample aged for 221 h at 23 °C can be drawn, as shown as the solid line in Figure 24.

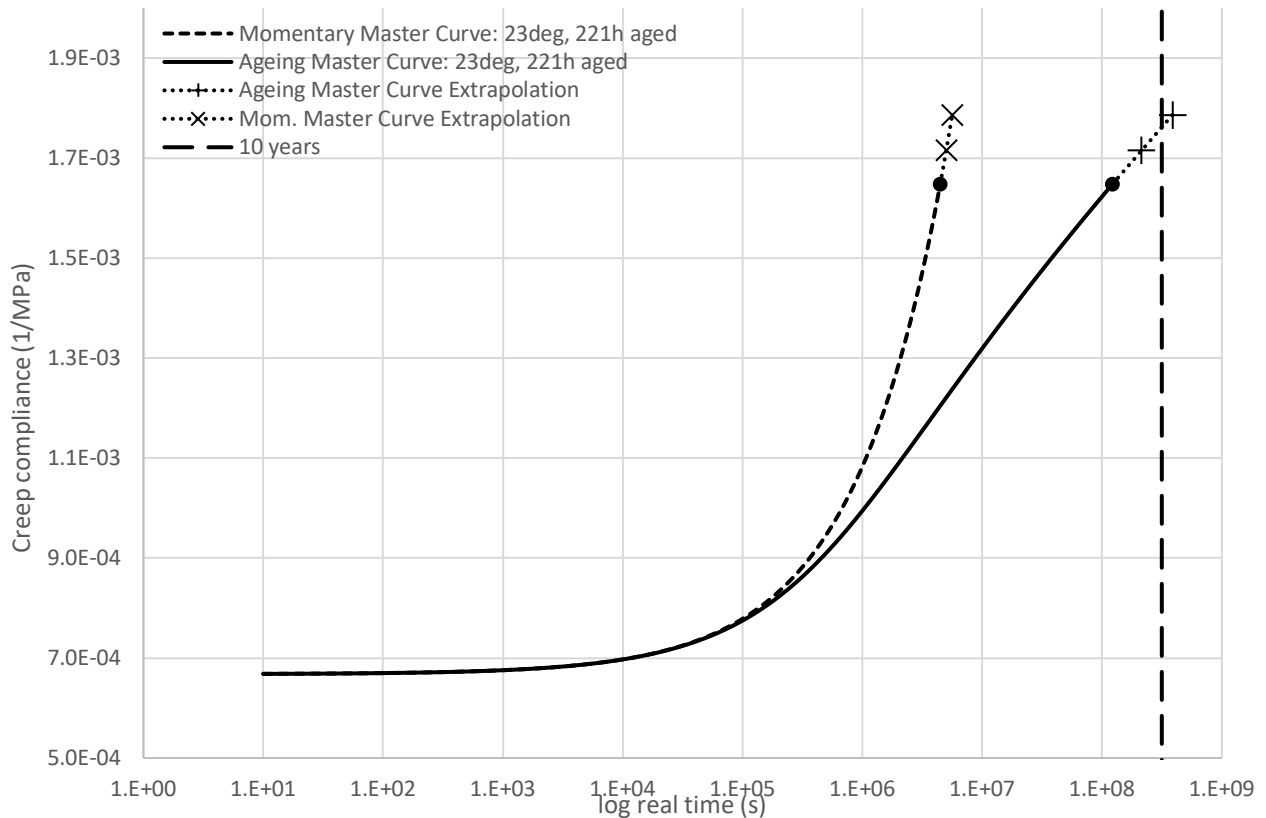


Figure 24: The momentary and ageing master curve for a sample aged for 221 h at 23 °C

The furthest points on the momentary and ageing master curves are highlighted by black dots in Figure 24. The longest age-affected creep behaviour prediction of additively manufactured PETG based on samples with an age of 221 h, is marked by the black dot on the ageing master curve: 3.88 years. Extrapolation of the momentary master curve with two data points, shown in Figure 24, is believed to be acceptable due to the smooth nature of the curves. This leads to an increase in the creep prediction of the ageing master curve to reach beyond 10 years.

5 Conclusion

Although PETG is widely used in the field of additive manufacturing, little information is available on the instantaneous mechanical properties, and even less data are available on its time-dependent properties. In particular, the prediction of the creep behaviour of additively manufactured PETG is an aspect where information is severely lacking. This article adds to the pool of knowledge in these areas while also presenting the constraints of the long-term creep prediction.

Regarding the instantaneous mechanical properties of additively manufactured PETG, the tensile experiments showed that the printed material exhibits a Young's modulus that is 86.5% of the theoretically possible value in direction 1. While the Young's modulus in direction 3 is within 1% of its theoretical maximum, the Young's modulus in direction 2 is only 66.0% of the theoretical optimum. The calculated shear moduli showed similar results with weaker shear properties in shear direction 13 compared with the others. The density of the feedstock was found to be

1292.6 kg/m³ and that of the extruded material was 1274.2 kg/m³.

Several findings regarding the time-dependent properties are:

- (1) The end of the linear viscoelastic range, in which the TTSP method of creep prediction can be applied, was found to be 1.09 kg for a 3 mm thick sample at 75 °C. However, the application of such a load on a creep sample at 70 °C resulted in failure of the sample after roughly 15 min, indicating that limiting the load to the end of the linear viscoelastic range does not exclude other failure modes from arising in the case of additively manufactured PETG.
- (2) Given the poor curve fitting of the vertical ageing shift factor $b(T)$, care should be taken when creating a master curve at temperatures other than those measured. Additional data points could improve the curve fit and more experiments in this area are recommended.
- (3) The creep experiments conducted at 65 °C did not superimpose on the lower temperature experiments, which indicates that the additively manufactured PETG stops acting in a rheologically-simple manner at this temperature and above. The results cannot contribute to the master curve since a rheologically-simple manner is the requirement of the TTSP creep prediction technique. Thus, the time span of the ageing master curve is capped so extrapolation of the ageing master curve beyond 3.88 years is a necessity if further creep prediction is required for the samples. Given the smooth nature of the ageing master curve, such extrapolation to 10 years is deemed to be acceptable in this research.

Despite the observed limiting factors above, the TTSP method of creep prediction has been successfully applied to additively manufactured PETG resulting in a novel creep prediction. The application of other creep prediction methodologies to additively manufactured PETG could gain further insights.

6 Declarations

6.1 Funding

The research study described herein is supported by an Australian Government Research Training Program Scholarship and is co-funded by the Department of Industry, Innovation and Science (Innovative Manufacturing CRC Ltd), the University of Technology Sydney (UTS) and Downer, via its subsidiary Mineral Technologies Pty Ltd (IMCRC/MTC/290418). The funding bodies were not involved in the study design; in the collection, analysis and interpretation of data; in the writing of the report; or in the decision to submit the article for publication.

6.2 Conflicts of interest/Competing interests

None.

7 Acknowledgment

The research study described herein is supported by an Australian Government Research Training Program Scholarship and is a collaboration between the University of Technology Sydney (UTS), the Innovative Manufacturing Cooperative Research Centre (IMCRC) and Downer, via its subsidiary Mineral Technologies. Thank you to UTS:Rapido, particularly, Hervé Harvard for establishing the research activity. The researchers would like to thank Samuel Gallagher, Samir Djulamerovic, Martin Do and Alexander Perry for all their efforts in conducting the experiments.

References

- [1] ASTM International, Additive manufacturing: General principles: Terminology, ASTM International, West Conshohocken, PA, 2015.
- [2] W. Zhang, C. Cotton, J. Sun, D. Heider, B. Gu, B. Sun, T.-W. Chou, Interfacial bonding strength of short carbon fiber/acrylonitrile-butadiene-styrene composites fabricated by fused deposition modeling, *Composites Part B: Engineering* 137 (2018) 51-59.
- [3] X. Liu, V. Shapiro, Homogenization of material properties in additively manufactured structures, *CAD Computer Aided Design* 78 (2016) 71-82.
- [4] J.R.C. Dizon, A.H. Espera, Q. Chen, R.C. Advincula, Mechanical characterization of 3D-printed polymers, *Additive Manufacturing* 20 (2018) 44-67.
- [5] B.H. Lee, J. Abdullah, Z.A. Khan, Optimization of rapid prototyping parameters for production of flexible ABS object, *Journal of Materials Processing Technology* 169(1) (2005) 54-61.
- [6] A.K. Sood, R.K. Ohdar, S.S. Mahapatra, Parametric appraisal of mechanical property of fused deposition modelling processed parts, *Materials & Design* 31(1) (2010) 287-295.
- [7] C. Casavola, A. Cazzato, V. Moramarco, C. Pappalettere, Orthotropic mechanical properties of fused deposition modelling parts described by classical laminate theory, *Materials & Design* 90 (2016) 453-458.
- [8] M. Somireddy, A. Czekanski, C.V. Singh, Development of constitutive material model of 3D printed structure via FDM, *Materials Today Communications* 15 (2018) 143-152.
- [9] M. Domingo-Espin, J.M. Puigoriol-Forcada, A.-A. Garcia-Granada, J. Llumà, S. Borros, G. Reyes, Mechanical property characterization and simulation of fused deposition modeling Polycarbonate parts, *Materials & Design* 83 (2015) 670-677.
- [10] A. Bellini, S. Güçeri, Mechanical characterization of parts fabricated using fused deposition modeling, *Rapid Prototyping Journal* 9 (2003) 252-264.
- [11] C.G. Amza, A. Zapciu, G. Constantin, F. Baciuc, M.I. Vasile, Enhancing Mechanical Properties of Polymer 3D Printed Parts, *Polymers* 13(4) (2021) 562.
- [12] K. Wang, J. Shen, Z. Ma, Y. Zhang, N. Xu, S. Pang, Preparation and Properties of Poly(ethylene glycol-co-cyclohexane-1,4-dimethanol terephthalate)/Polyglycolic Acid (PETG/PGA) Blends, *Polymers* 13 (2021) 452.
- [13] R.B. Dupaix, M.C. Boyce, Finite strain behavior of poly(ethylene terephthalate) (PET) and poly(ethylene terephthalate)-glycol (PETG), *Polymer* 46(13) (2005) 4827-4838.
- [14] M. Kattan, E. Dargent, J. Ledru, J. Grenet, Strain-induced crystallization in uniaxially drawn PETG plates, *Journal of Applied Polymer Science* 81(14) (2001) 3405-3412.
- [15] K. Upadhyay, R. Dwivedi, A.K. Singh, Determination and Comparison of the Anisotropic Strengths of Fused Deposition Modeling P400 ABS, in: D.I. Wimpenny, P.M. Pandey, L.J. Kumar (Eds.), *Advances in 3D Printing & Additive Manufacturing Technologies*, Springer Singapore, Singapore, 2017, pp. 9-28.
- [16] N. Aliheidari, J. Christ, R. Tripuraneni, S. Nadimpalli, A. Ameli, Interlayer adhesion and fracture resistance of polymers printed through melt extrusion additive manufacturing process, *Materials & Design* 156 (2018) 351-361.
- [17] A. Arivazhagan, S.H. Masood, I. Sbarski, Dynamic mechanical analysis of fused deposition modelling processed polycarbonate, 69th Annual Technical Conference of the Society of Plastics Engineers (ANTEC 2011), Boston, USA, 2011, pp. 950-955.
- [18] L.C.E. Struik, *Physical Aging In Amorphous Polymers and Other Materials*, Technische Hogeschool Delft, 1978.
- [19] E.J. Barbero, Time-temperature-age superposition principle for predicting long-term response of linear viscoelastic materials, in: R.M. Guedes (Ed.), *Creep and Fatigue in Polymer Matrix Composites*, Woodhead Publishing 2011, pp. 48-69.
- [20] E.R. Pierik, W.J.B. Grouve, M. van Drongelen, R. Akkerman, The influence of physical ageing on the in-plane shear creep compliance of 5HS C/PPS, *Mechanics of Time-Dependent Materials* 24 (2019) 197-220.
- [21] O.A. Mohamed, S.H. Masood, J.L. Bhowmik, Influence of processing parameters on creep and recovery behavior of FDM manufactured part using definitive screening design and ANN, *Rapid Prototyping Journal* 23(6) (2017) 998-1010.

- [22] O.A. Mohamed, S.H. Masood, J.L. Bhowmik, Experimental investigation of time-dependent mechanical properties of PC-ABS prototypes processed by FDM additive manufacturing process, *Materials Letters* 193 (2017) 58-62.
- [23] D.-A. Türk, F. Brenni, M. Zogg, M. Meboldt, Mechanical characterization of 3D printed polymers for fiber reinforced polymers processing, *Materials & Design* 118 (2017) 256-265.
- [24] I. Shaheer, Characterization of Viscoelastic Properties of a Material Used for an Additive Manufacturing Method, University of North Texas Denton, Texas, 2013.
- [25] A.G. Salazar-Martín, M.A. Pérez, A.A. García-Granada, G. Reyes, J.M. Puigoriol-Forcada, A study of creep in polycarbonate fused deposition modelling parts, *Materials & Design* 141 (2018) 414-425.
- [26] T. Romeijn, K. Singh, M. Behrens, G. Paul, Effect of accelerated weathering on the creep behaviour of additively manufactured Polyethylene Terephthalate Glycol (PETG), *Journal of Polymer Research* 28 (2021) Article 352.
- [27] C.G. Amza, A. Zapciu, F. Baciú, M.I. Vasile, A.I. Nicoara, Accelerated Aging Effect on Mechanical Properties of Common 3D-Printing Polymers, *Polymers* 13(23) (2021) 4132.
- [28] ASTM International, Standard Test Method for Tensile Properties of Polymer Matrix Composite Materials, ASTM International, West Conshohocken, PA, 2014.
- [29] T. Romeijn, B. Wells, D. Wei, G. Paul, Investigation into the shear property of thin-walled additively manufactured structures using staggered fused filament fabrication, *Additive Manufacturing* 35 (2020) Article 101259.
- [30] H. Izadi Gonabadi, Y. Chen, A. Yadav, S. Bull, Investigation of the effect of raster angle, build orientation, and infill density on the elastic response of 3D printed parts using finite element microstructural modeling and homogenization techniques, *The International Journal of Advanced Manufacturing Technology* 118 (2021) 1485–1510.
- [31] Y. Zhao, Y. Chen, Y. Zhou, Novel mechanical models of tensile strength and elastic property of FDM AM PLA materials: Experimental and theoretical analyses, *Materials & Design* 181 (2019) Article 108089.
- [32] L. Li, Q. Sun, C. Bellehumeur, P. Gu, Composite Modeling and Analysis for Fabrication of FDM Prototypes with Locally Controlled Properties, *Journal of Manufacturing Processes* 4(2) (2002) 129-141.
- [33] G. Alaimo, S. Marconi, L. Costato, F. Auricchio, Influence of meso-structure and chemical composition on FDM 3D-printed parts, *Composites Part B: Engineering* 113 (2017) 371-380.
- [34] N. Dialami, M. Chiumenti, M. Cervera, R. Rossi, U. Chasco Goñi, M. Domingo, Numerical and experimental analysis of the structural performance of AM components built by Fused Filament Fabrication, *International Journal of Mechanics and Materials in Design* 17 (2021) 225–244.
- [35] G.Z. Voyiadjis, P.I. Kattan, *Mechanics of Composite Materials with MATLAB*, Springer Berlin Heidelberg 2005.
- [36] H. Leaderman, *Elastic and creep properties of filamentous materials and other high polymers*, The Textile Foundation, 1943.
- [37] A.V. Tobolsky, R.D. Andrews, Systems Manifesting Superposed Elastic and Viscous Behavior, *The Journal of Chemical Physics* 13(1) (1945) 3-27.
- [38] H. Peng, J. Jiang, J. Lu, J. Cao, Application of time–temperature superposition principle to Chinese fir orthotropic creep, *J. Wood Sci.* 63(5) (2017) 455-463.
- [39] R.M. Guedes, J.L. Morais, A simple and effective scheme for data reduction of stress relaxation incorporating physical-aging effects: An analytical and numerical analysis, *Polymer Testing* 32(5) (2013) 961-971.
- [40] M. Hadid, S. Rechak, A. Zouani, Empirical nonlinear viscoelastic model for injection molded thermoplastic composite, *Polymer Composites* 23(5) (2002) 771-778.
- [41] J. Bergström, Linear Viscoelasticity, *Mechanics of Solid Polymers* 2015, pp. 309-351.
- [42] ASTM International, Standard Test Methods for Tensile, Compressive, and Flexural Creep and Creep-Rupture of Plastics, ASTM International, West Conshohocken, PA, 2017.
- [43] A.A. Qaiser, J. Price, Estimation of long-term creep behavior of polycarbonate by stress-time superposition and effects of physical aging, *Mechanics of Time-Dependent Materials* 15(1) (2011) 41-50.
- [44] W.J. Liou, C.I. Tseng, Creep behavior of nylon-6 thermoplastic composites, *Polymer Composites* 18(4) (1997) 492-499.

- [45] J. Kolařík, A. Pegoretti, Non-linear tensile creep of polypropylene: Time-strain superposition and creep prediction, *Polymer* 47(1) (2006) 346-356.
- [46] J. Bergström, *Experimental Characterization Techniques, Mechanics of Solid Polymers* 2015, pp. 19-114.
- [47] TA Instruments, Determination of the Linear Viscoelastic Region of a Polymer using a Strain Sweep on the DMA 2980, *Thermal Analysis & Rheology*, n.d.
- [48] S.B. Rayhan, M. Rahman, Modeling elastic properties of unidirectional composite materials using Ansys Material Designer, *Procedia Structural Integrity* 28 (2020) 1892-1900.
- [49] M. Rahman, S.B. Rayhan, Impact of Micromechanical and Carbon Fiber Properties on the Elastic Modulus of CFRP Woven Composites, in: L. Zheng, C. Sun, K.-L. Goh (Eds.) *Proceedings of MEACM 2020*, Springer International Publishing, Cham, 2021, pp. 295-303.
- [50] S. Andrews Zachariah, B. Satish Shenoy, K. Dayananda Pai, Comprehensive analysis of in-plane tensile characteristics of thin carbon/aramid hybrid composites using experimental and RVE-based numerical study, *Composite Structures* 271 (2021) 114160.
- [51] S. Hadiouch, M. Maresca, D. Gigmès, G. Machado, A. Maurel-Pantel, S. Frik, J. Saunier, A. Deniset-Besseau, N. Yagoubi, L. Michalek, C. Barner-Kowollik, Y. Guillaneuf, C. Lefay, A versatile and straightforward process to turn plastics into antibacterial materials, *Polymer Chemistry* 13(1) (2022) 69-79.
- [52] E.J. Barbero, Prediction of Long-term Creep of Composites from Doubly-shifted Polymer Creep Data, *Journal of Composite Materials* 43(19) (2009) 2109-2124.
- [53] E.J. Barbero, K.J. Ford, Equivalent Time Temperature Model for Physical Aging and Temperature Effects on Polymer Creep and Relaxation, *Journal of Engineering Materials and Technology* 126(4) (2004) 413-419.
- [54] A. Maiti, A geometry-based approach to determining time-temperature superposition shifts in aging experiments, *Rheologica Acta* 55(1) (2016) 83-90.
- [55] M.L. Williams, R.F. Landel, J.D. Ferry, The Temperature Dependence of Relaxation Mechanisms in Amorphous Polymers and Other Glass-forming Liquids, *Journal of the American Chemical Society* 77(14) (1955) 3701-3707.
- [56] J.L. Sullivan, E.J. Blais, D. Houston, Physical aging in the creep behavior of thermosetting and thermoplastic composites, *Composites science and technology* 47(4) (1993) 389-403.
- [57] R.D. Bradshaw, L.C. Brinson, Physical aging in polymers and polymer composites: An analysis and method for time-aging time superposition, *Polymer engineering and science* 37(1) (1997) 31-44.
- [58] R.D. Bradshaw, L.C. Brinson, A continuous test data method to determine a reference curve and shift rate for isothermal physical aging, *Polymer engineering and science* 39(2) (1999) 211-235.